J. Fluid Mech. (2000), *vol.* 413, *pp.* 111–148. Printed in the United Kingdom

The motion generated by a rising particle in a rotating fluid — numerical solutions. Part 1. A short container

By E. MINKOV, M. UNGARISH† AND M. ISRAELI

Computer Science Department, Technion – Israel Institute of Technology, Haifa 32000, Israel

(Received 8 February 1999 and in revised form 21 January 2000)

Numerical finite-difference results of the full axisymmetric incompressible Navier–Stokes equations are presented for the problem of the slow axial motion of a disk particle in an incompressible, rotating fluid in a cylindrical container. The governing parameters are the Ekman number, E, the Rossby number, Ro, and the dimensionless height of the container, H (with respect to the diameter of the particle). The study concerns small values of E, Ro, and $HE^{-1/2}$ and compares the numerical results with predictions of previous analytical (mostly approximate) studies. Special attention is focused on the drag force. First, developed (quasi-steady state) cases are considered. Excellent agreement with the exact linear ($Ro = 0$) solution of Ungarish & Vedensky (1995) is obtained when the computational $Ro = 10^{-4}$. The effects of the nonlinear momentum advection terms are analysed and shown to be proportional to $RoE^{-1/2}$. Next, the time-development for both (*a*) impulsive start and (*b*) start under a constant axial force are considered, and good qualitative agreement with previous analytical results (including the appearance of oscillations in case (*b*)) is indicated.

1. Introduction

We consider the slow axial motion of a symmetrical particle, whose circumscribing cylinder is of radius a^* in an incompressible, rotating fluid in a cylindrical container of length $2H^*$ and radius r^*_{max} which rotates with high angular velocity Ω^* around the axis of symmetry, z, as sketched in figure 1. The particle axial velocity relative to the container is denoted by w^*_p and its (quasi) steady-state value W^* will be used as the reference velocity. Typically, the considered particle is in the middle of the container. We are interested in the velocity field and drag force, D^*. The asterisk denotes a dimensional variable.

This problem is fundamental to the theory of rotating fluids and incorporates many variants of the essential ingredients of the topic: Ekman and Stewartson layers, the Taylor column, the linear theory, inertial modifications, and more (see Greenspan 1968). From the academic aspect, this problem deserves attention because there still are gaps in knowledge and some intriguing discrepancies between theory and experiments. Applications of the results are expected in investigations of the rheology of rotating suspensions, centrifugal separation processes and the motion of cores of planets. However, numerical simulations of this problem are conspicuously lacking.

† Author to whom correspondence should be addressed.

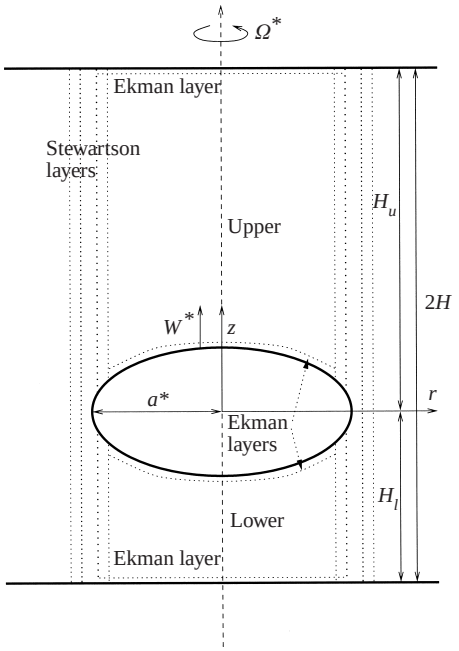

FIGURE 1. Sketch of the configuration. The particle is solid and torque-free (in the present investigation, a thin disk). The boundaries of the cylindrical container co-rotate with the coordinate system; the lateral boundary which is at $r = r_{max}$ is not shown here. In the 'long' container the Stewartson layers tend to merge into a free Taylor column. a^*, W^* and a^*/W^* are the scales for length, velocity and time t. (In addition to t, the dimensionless time $\mathscr{T}$ which is scaled with Ω^{*-1} is also used.) The z- and r-directions are called 'vertical' and 'horizontal'.

The equations governing the motion of an incompressible viscous fluid, in a system rotating with constant angular velocity Ω^*, are the conservation of mass and momentum:

$$\nabla \cdot \boldsymbol{v}^* = 0, \tag{1.1}$$

$$\frac{\partial \boldsymbol{v}^*}{\partial t^*} + \boldsymbol{v}^* \cdot \nabla \boldsymbol{v}^* + 2\boldsymbol{\Omega}^* \times \boldsymbol{v}^* = -\frac{\nabla p^*}{\rho^*} - \nu^* \nabla \times \nabla \times \boldsymbol{v}^*. \tag{1.2}$$

Here, $\boldsymbol{v}^*$ is the velocity in the rotating coordinate system, p^* is the reduced pressure, t^* is time, ρ^* and ν^* are the density and kinematic viscosity of the fluid. We attach the origin of the coordinate system to the centre of the particle, and denote by z the axial coordinate, pointing in the direction of $\boldsymbol{\Omega}^*$. We note that if the origin of the coordinate system (the particle) is accelerated by $A^*(t)$ in the z-direction and/or the gravity acceleration g^* acts in the $-z$-direction, then the reduced pressure p^* also contains the term $\rho^*[g^* + A^*(t)]z^*$ in addition to the centrifugal term, but the equations remain unchanged. We emphasize that the coordinate system is attached to the particle only concerning the axial motion, but it rotates with the constant Ω^* of the container boundaries, which may be different from that of the particle.

The main dimensionless parameters highlighting the flow field generated by the motion of the particle are

$$E = \frac{\nu^*}{\Omega^* a^{*2}}, \qquad Ro = \frac{W^*}{\Omega^* a^*} \qquad \text{and} \qquad H = \frac{H^*}{a^*}. \tag{1.3}$$

The Ekman number, E, expresses the typical ratio of the viscous to the Coriolis force in the fluid. It is also common to use the Taylor number, $T = 1/E$, in this context. We are interested in flows with small E (large T). The Rossby number, Ro, expresses the ratio of the inertial and advective to the Coriolis accelerations in the fluid, and provides an estimate of the relative importance of the nonlinear terms in the equations of motion. The aspect ratio, or dimensionless height, H, is a geometric parameter, but, as detailed below, its magnitude relative to $E^{-1/2}$ has a major influence in determining the characteristics of the flow field. In this paper we consider the case of $H \ll E^{-1/2}$ (to be more specific, $0.01 \leqslant HE^{1/2} \leqslant 0.13$).

To non-dimensionalize the equations (1.1)–(1.2) and the drag force the following scaling is utilized:

$$\{\boldsymbol{r}^*, t^*, \boldsymbol{v}^*, p^*, D^*\} = \left\{a^*\boldsymbol{r}, \frac{a^*}{W^*}t, W^*\boldsymbol{v}, \frac{W^*v^*\rho^*}{a^*}p, W^*v^*\rho^*a^*D\right\}. \tag{1.4}$$

Now the governing equations read

$$\nabla \cdot \boldsymbol{v} = 0, \tag{1.5}$$

$$Ro\frac{\partial \boldsymbol{v}}{\partial t} + Ro\,\boldsymbol{v}\cdot\nabla\boldsymbol{v} + 2\hat{\boldsymbol{z}} \times \boldsymbol{v} = -E\nabla p - E\nabla \times \nabla \times \boldsymbol{v}, \tag{1.6}$$

where $\hat{\boldsymbol{z}}$ is the unit vector in the direction of the axis of rotation. Setting $Ro = 0$ in equation (1.6) yields the important linear formulation, which was adopted in most of the previous pertinent theoretical investigations.

The boundary conditions are no-penetration and no-slip on the particle, whose geometry is specified, and on the container boundaries (in some analytical investigations the boundaries of the container are assumed to be 'at infinity'). The angular motion of the particle itself is defined by the condition that no external torque is applied on the particle. The vertical motion of the particle is defined as follows. In the case when the (quasi) steady-state motion is of interest the vertical velocity of the particle is set to be constant. In the case when the time-dependent transient flow field is of interest, two situations are considered: (*a*) impulsive set up of the velocity to a constant value, which significantly simplifies the investigation, or (*b*) calculation of the accelerated motion of the particle from rest under the action of a constant axial driving force, which simulates the behaviour of a buoyant particle in a gravity field parallel to the axis of rotation.

It is both mathematically and physically convenient to distinguish between two major cases: the 'short' and 'long' container types of flow field. The former is expected when $H \ll E^{-1/2}$, in which case the flow field is dominated by the Ekman layers and the dimensionless drag force on the particle is $O(E^{-3/2})$. In the latter, expected when $H > 0.05E^{-1}$, the fascinating free Taylor column structure appears and the drag force is $O(E^{-1})$. The numerical method of solution described below turns out to be applicable to both configurations subject to some minor adaptations. However, for focusing the discussion, we have separated the investigation of these cases. The present paper is concerned with the short container, and a sequel paper (Minkov, Ungarish & Israeli 2000) will describe the results for the long container.

1.1. *Previous investigations*

Here we present a brief summary of previous studies on the short container configuration. More details will be given in the next sections during the discussion of our new results.

The analytical results (with an exception that will be specified) were based on the linear theory (i.e. $Ro = 0$ multiplies all advection terms in the momentum equations). This simplification still leaves a formidable system and additional approximations and restrictions were necessary for progress.

The approximate solutions are for the asymptotic $E \to 0$ limit. Stewartson (1966) and Moore & Saffman (1968, 1969) considered the steady-state flow over a solid particle, and showed that the flow field consists of z-independent geostrophic 'cores', Ekman boundary layers on the particle and horizontal boundaries and Stewartson shear layer on the cylinder circumscribing the solid particle. The details, in particular of the inner Stewartson $E^{1/3}$ layer, are still too complicated for detailed calculations in cases of interest. A simple and robust further approximation is the 'geostrophic' model that neglects the influence of the Stewartson layers (actually it implies that the thickness of the vertical shear layers is zero and no radial motion of the fluid takes place outside the Ekman layers). The geostrophic model provides a simple analytical formula for the drag force, which is a variable of major concern in practical applications and in experimental measurements. Moore & Saffman's (1968) result for the geostrophic drag for a rigid sphere is

$$D_0^* = \tfrac{43}{105}\pi E^{-3/2}(W^* v^* \rho^* a^*),$$

and hence, in dimensionless form,

$$D_0 = \tfrac{43}{105}\pi E^{-3/2} \tag{1.7}$$

(the subscript 0 is used to denote the geostrophic drag; for a disk the coefficient $\frac{43}{105}$ should be replaced by $\frac{1}{2}$). We emphasize that the geostrophic drag is independent of H and also of the position of the particle between the horizontal boundaries.

Maxworthy (1968) performed experiments in order to verify the results of Moore & Saffman (1968). He used a container 40 cm long, 28 cm in diameter filled with water, in which buoyant spheres, of diameters 1.9 and 3.9 cm, were released along the axis. The drag force was calculated from the measured time of motion between two marks 25 cm apart, and observations of the flow were carried out by colouring selected regions. Even for the smallest value of Ro the drag was about 20% below the theoretical D_0 and significant differences from the geostrophic flow field (in particular a radial flow outside the Ekman layers) were observed. Maxworthy, using an order-of-magnitude argument of Moore & Saffman, attributed these discrepancies to the effect of the nonlinear advection terms, and inferred that only for $Ro < 10^{-3}E^{2/3}$ can a good agreement (of about 2.5%) between theory and experiment be realized. In other words, this suggested that the errors of the linear theory are of magnitude $10RoE^{-2/3}$. The limitation of the linear theory to such extremely small values of Ro, about 100 times smaller than achieved in the experiment, cast serious doubts on the applicability of the linear theory to this type of problem.

Bush, Stone & Bloxham (1992, 1995) extended the geostrophic results to the case of buoyant bubbles or drops in circumstances which allow for decoupling between shape and motion, and derived the corresponding geostrophic drag force formula which is similar to (1.7) but with the leading coefficient increasing from $\frac{43}{105}$ to 1 as the no-slip parameter (the transport efficiency of the Ekman layer on the drop interface relative to a similar solid surface) decreases from 1 to 0. Bush *et al.* (1995) also performed relevant experiments which, again, show that the actual drag force is significantly smaller than the geostrophic prediction.

Ungarish & Vedensky (1995) derived, by Hankel transform methods, an 'exact' solution of the linear equations which is, however, limited to a very special configuration: the (quasi) steady motion of the disk in the midplane of a container of infinite r_{max}. They showed that the exact linear drag force is dependent on the value of H (unlike the geostrophic drag) and, for the values of E and H used in Maxworthy's experiment, the exact linear drag force is considerably smaller than the prediction of the geostrophic approximation. They suggested that the discrepancies reported by Maxworthy should be mainly attributed to the lack of Stewartson layers effects in the geostrophic result, not to the lack of advection terms. Quantitative comparisons could not be performed because of the different geometries.

Ungarish (1996) developed the 'quasi-geostrophic' model which assumes that the $E^{1/3}$ Stewartson layer is negligibly thin, but incorporates, in addition to the Ekman layers (as in the geostrophic model), also the viscous effects in the (extended) $E^{1/4}$-type Stewartson layers. This allows for a radial flow outside the Ekman layers, consistent with experimental observations. The flow field and drag force can still be obtained by relatively simple calculations. The resulting quasi-geostrophic drag force is dependent also on H and, for a solid spherical particle in the proper parameter range, is smaller than the experimental values of Maxworthy by about 20%–30%. The discrepancies were attributed to the lack of $E^{1/3}$ layers effect. The discrepancy with the experimental results of Bush *et al.* (1995) for drops is even larger, but the $E^{1/3}$ layers in the parameter range of these experiments are really thick.

Ungarish (1996) also used the quasi-geostrophic model for deriving a quantitative estimate of the contribution of the nonlinear terms to the flow field when Ro is small but not zero. The analysis indicated that the 'effective' Rossby number is $RoE^{-1/2}$, and that the drag force decreases (but only slightly) due to the inertial effects when this parameter is small. This strengthened the inference that the reported discrepancy between the geostrophic theory and experiments does not necessarily mean that the linear theory is wrong, but rather that the geostrophic approximation is not accurate.

The time-dependent flow field generated by a particle in a rotating fluid in the short container configuration has received little attention. It was considered briefly by Smith (1987), and in more detail by Ungarish (1997). The last work considers, in the framework of the geostrophic and quasi-geostrophic models, the behaviour of the flow field and drag force for both an impulsive start and a start under constant external force. For the latter case some strong oscillations of the axial velocity were predicted which are, however, inconsistent with some of the underlaying assumptions of the models. No experimental or theoretical support for these results was available.

1.2. *Objectives*

The evident parametric limitations of the abovementioned theoretical studies – and in particular the apparently poor agreement with experiments, the complete lack of experimental evidence for the time-dependent motion, and the lack of numerical solutions – give rise to confusion and cast doubt on the reliability of the body of knowledge concerning this problem. The most pressing issues are the effect of the advective nonlinear terms when Ro is small but finite and the time-dependent behaviour.

In the present study we intended to throw some light on these topics. To this end, we attempted the numerical solutions of the full system of Navier–Stokes equations (1.5)–(1.6) for a disk particle, by a finite difference method. The advantage over the previous investigations is the incorporation of all known physical effects in the analysis. We are therefore able to gain wider, more reliable and more accurate results

and insights. To the best of our knowledge, no such numerical results have been published before (Dennis *et al.* 1982 attempted a related numerical solutions for a sphere in an unbounded domain but, due to convergence difficulties, presented results only for large values of the Ekman number). The main restrictions on our study stem from the following. (*a*) The *a priori* enforcement of axisymmetry. This assumption, however, is expected to be relevant to many real flows. (*b*) The special geometry of the particle. There are many theoretical indications that the essential flow-field features for spherical, ellipsoidal and disk particles are very similar, and that this similarity increases with H, but of course future computations for these shapes are necessary.

The first objective was to assess the validity of previous 'exact' (quasi) steady-state linear solutions (obtained by Ungarish & Vedensky 1995) via a comparison with the present numerical results (for very small Ro). The comparison covered both the flow field and the drag force. The second objective was to investigate the influence of the inertial terms on the flow field and the drag force. This enabled us to estimate the range of applicability of the linear theory results, i.e. the link between the value of the parameter Ro and the deviation from the prediction of the linear theory (in particular, for the drag force).

The next objective was the investigation of the time-dependent behaviour of the flow field for which very little information was available. This has been performed for two types of forcing: (*a*) impulsive start from rest (in the rotating system) and (*b*) start from rest (in the rotating system) under a constant force.

The corresponding numerical results and the comparison with previous theoretical knowledge are presented and discussed below. The paper is organized as follows. The numerical finite-difference approach is introduced in § 2. The numerical results for developed flow fields (i.e. in quasi-steady state) are presented and discussed in § 3, first for the linear case ($Ro = 10^{-4}$ in the numerical solution), then for nonlinear cases (up to $RoE^{-1/2} = 0.8$). The time-dependent motion is considered in § 4. We present some concluding remarks in § 5.

2. The numerical scheme

2.1. *Formulations*

We solve numerically the full system of Navier–Stokes equations in the rotating system, (1.5)–(1.6), in the configuration depicted in figure 1 for a disk-shaped particle. In view of the axial symmetry, the scalar form of the governing equations is

$$Ro\left(\frac{\partial u}{\partial t}+u\frac{\partial u}{\partial r}-\frac{v^2}{r}+w\frac{\partial u}{\partial z}\right)-2v=-E\frac{\partial p}{\partial r}+E\left(\nabla^2-\frac{1}{r^2}\right)u, \tag{2.8}$$

$$Ro\left(\frac{\partial v}{\partial t}+u\frac{\partial v}{\partial r}+\frac{uv}{r}+w\frac{\partial v}{\partial z}\right)+2u=E\left(\nabla^2-\frac{1}{r^2}\right)v, \tag{2.9}$$

$$Ro\left(\frac{\partial w}{\partial t}+u\frac{\partial w}{\partial r}+w\frac{\partial w}{\partial z}\right)=-E\frac{\partial p}{\partial z}+E\nabla^2 w, \tag{2.10}$$

$$\frac{1}{r}\frac{\partial(ur)}{\partial r}+\frac{\partial w}{\partial z}=0, \tag{2.11}$$

where

$$\nabla^2=\frac{\partial^2}{\partial r^2}+\frac{1}{r}\frac{\partial}{\partial r}+\frac{\partial^2}{\partial z^2}.$$

Here r and z are the radial and axial coordinates in a cylindrical frame attached to the centre of the disk and rotating with the walls and $\{u, v, w\}$ are the velocity components.

The boundary conditions on the disk and the walls are specified as

$$u = w = 0; \qquad v = r\omega_p \quad \text{at } 0 \leqslant r \leqslant 1, \quad z = 0; \tag{2.12}$$

$$u = v = 0; \qquad w = -w_p \quad \text{at } z = H_u, -H_l; \tag{2.13}$$

$$u = v = 0; \qquad \frac{\partial w}{\partial r} = 0 \quad \text{at } r = 0; \tag{2.14}$$

$$u = v = 0; \qquad w = -w_p \quad \text{at } r = r_{max}. \tag{2.15}$$

Here H_u, H_l are the heights of upper and lower domains with respect to the particle, r_{max} is the radius of the container, w_p is the vertical velocity of the particle relative to the boundary and ω_p is the angular velocity of the particle. The value of ω_p is not prescribed, but a consequence of the condition that no external torque is applied on the disk. This is expressed by the auxiliary equation:

$$\int_0^1 \left(\left.\frac{\partial v}{\partial z}\right|_{z=0+} - \left.\frac{\partial v}{\partial z}\right|_{z=0-} \right) r^2 \, \mathrm{d}r = 0, \tag{2.16}$$

which becomes a part of the system which we attempt to solve. For the value of w_p we considered two cases. (*a*) The impulsive start from rest with constant velocity, for which we set simply $w_p = 1$. This is the default condition in the present investigation, and is used if not specified otherwise. (*b*) The release from rest under a constant axial force (we have in mind a model for a buoyant particle in a gravity field acting in the z-direction). In this case the determination of time-dependent w_p, from the equation of motion of the particle as described in § 4.2, is also a part of the problem.

The initial conditions at $t = 0$ are simply $\boldsymbol{v} = \boldsymbol{0}$ and a prescribed position $H_l(t = 0)$ of the particle. (Some modifications will be introduced and discussed later.)

For presentation purposes we introduce the stream function

$$\psi(r, z) = -\int_0^r r' w(r', z) \, \mathrm{d}r'. \tag{2.17}$$

The solution of the foregoing system is attempted with the finite-difference method, using explicit approximation in time of the viscous, Coriolis and nonlinear terms, and implicit approximation for the pressure, i.e. the flow field at the $(n + 1)$th time step is calculated from the flow field at the nth time step by adding the contribution of the linear and nonlinear momentum terms calculated explicitly at the nth time step and the contribution of the pressure gradient that is calculated implicitly from the condition of continuity, $\nabla \cdot \boldsymbol{v}^{n+1} = 0$. This requires the solution of a Poisson equation for each time step. The details are as follows.

2.2. *The grid structure*

We use a rectangular grid in the meridional plane (z, r) that is attached to the disk while the axis of the rotation (which is also the axis of symmetry) is located on the grid line $r = 0$; the disk is located on the grid line $z = 0$, from $r = 0$ to $r = 1$. The horizontal walls of the container (the upper and the lower planes) move with respect to the horizontal grid lines, see figure 2. The outer boundary of the grid is placed at $r = r_{max}$. We chose values of r_{max} large enough to have negligible influence on the flow. We expected and confirmed by numerical tests that for the short

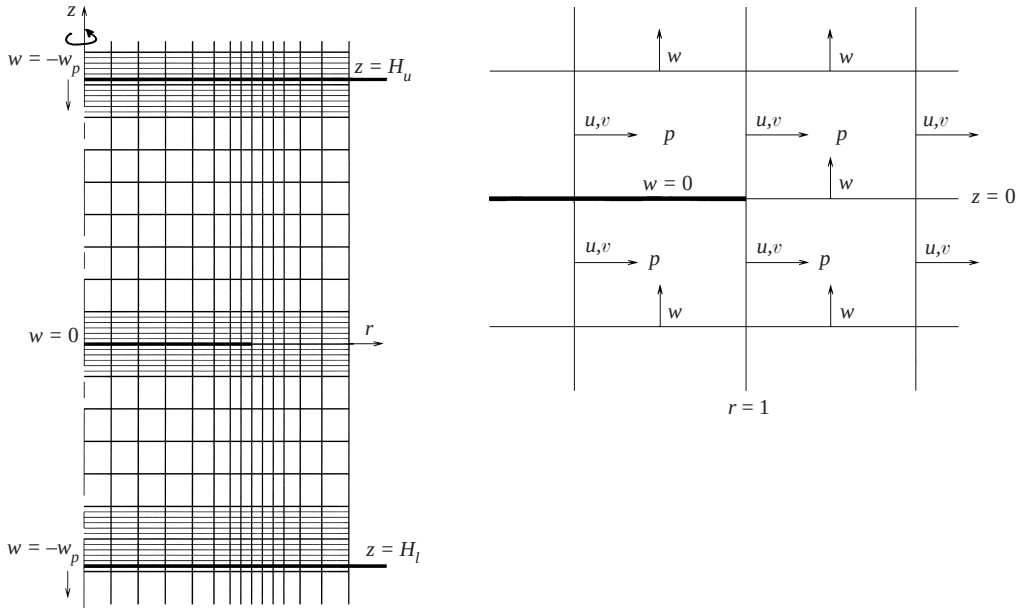

FIGURE 2. Schematic description of the grid and of the computational cells around the disk edge. The thick lines are horizontal boundaries. The grid is attached to the disk.

container configurations with $E \leqslant 10^{-3}$ and $H < 8$, in which the thickness of the outer Stewartson layer, $E^{1/4}H^{1/2}$, is less than 0.5, $r_{max} = 2$ is large enough for this purpose. For the long container configurations, where no clear-cut vertical layers appear, we have found by similar numerical tests that the appropriate value is $r_{max} = 5$; this will be discussed in the sequel paper.

The discretization grid is non-uniform, in an attempt to improve the resolution in the region around $r = 1$ and in the Ekman layers. For the radial coordinate we used the standard method of mapping of the physical domain into the computational one, by the function $f : [0, r_{max}] \to [0, 1]$

$$f(r) = \frac{r + (2/\pi)\left(\arctan\left((r-1)/E^{1/4}\right) + \arctan\left(1/E^{1/4}\right)\right)}{r_{max} + (2/\pi)\left(\arctan\left((r_{max}-1)/E^{1/4}\right) + \arctan\left(1/E^{1/4}\right)\right)}.$$

Equal intervals are taken in the computational domain. In this stretching the density of the vertical ($r = r_i$) grid lines changes smoothly; it is maximal in the Stewartson layers at $r = 1$ and decreases towards the centre and the outer boundary; about $1/(1 + 0.5r_{max})$ of the radial grid intervals are concentrated in a layer of thickness $2E^{1/4}$ around the cylinder $r = 1$.

On the other hand, for the definition of the grid in the axial direction we used a more sophisticated and non-standard approach which takes into account the relative motion between the particle and the boundaries. The z_j grid lines form two sub-grids: the 'main' grid and the 'fine' grid. The main grid is uniform in the z-direction; the interval Δz_{main} is larger than $E^{1/2}$ but still able to provide a good resolution for the flow field outside the Ekman layers. The fine grid is needed for the resolution of the Ekman layers on the horizontal walls and on the disk. Several layers of the main grid cells in these regions are refined by sub-division, so that the total thickness of the refined region is larger than the Ekman layer and the resolution in the Ekman

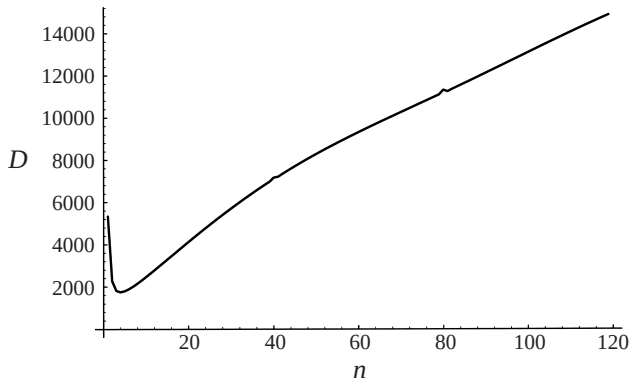

FIGURE 3. The drag force as a function of the number of time steps for $E = 10^{-3}$, $Ro = 10^{-2}$, $H = 1$. The axial grid is adjusted to the changing geometry by 'jumps' each 40 time steps. $\Delta t = 10^{-2}/60$. (This is an early stage of the solution and therefore a rapid variation of D still occurs.)

layers is satisfactory. The location of the refined regions near the horizontal walls with respect to the main grid (attached to the particle) varies with time as follows. Initially we refine a number of grid layers, say *div*, above and under the disk, $div + 1$ layers under the top wall, *div* layers above and one layer under the bottom wall. The time step Δt is chosen small enough to satisfy the requirement that the particle advances Δz_{fine} in several time steps; during these time steps the position of the walls is frozen, and the flow field is computed in this frozen geometry. After these several time steps the top and bottom walls are displaced one fine grid layer down (the thickness of the refined regions under the horizontal planes decreases). After several such small displacements, when the walls reach a line of the main grid (i.e. as they have moved a distance equal to Δz_{main}), the number of refined layers under the top plane becomes *div*, and the number of refined layers above the bottom plane becomes $div + 1$. Now we update the grids by refining one additional layer of the main grid in the top region and eliminating the refined layer of the main grid in the bottom region. A new cycle begins in which the motion of the boundary is again as described above. (The grid layers that accumulate above the top boundary are discarded.)

We emphasize that $\Delta z_{\text{fine}} \ll 1$ and hence the 'jump' of the container walls once in several time steps is not expected to affect significantly the smoothness of the computed flow-field variables. This was indeed observed in the results, and an example is shown in figure 3, which depicts the behaviour of the drag force vs. the number of time steps for the configuration $E = 10^{-3}$, $Ro = 10^{-2}$, $H = 1$ and $r_{max} = 2$, with the disk initially placed in the middle of the container. The grid has 60 intervals in the r-direction and 60 main-grid layers in the z-direction, $\Delta z_{\text{main}} = \frac{1}{30}$. With $div = 2$, the corresponding number of layers near the disk and the horizontal planes are each sub-divided into five sub-layers, i.e. $\Delta z_{\text{fine}} = \frac{1}{150}$. The time step $\Delta t = 10^{-2}/60$ causes a jump of the grid every 40 time steps, and a new refinement every 200 time steps. We can see that the effect of the perturbation created by each jump is small and decays very quickly, in about three time steps.

2.3. *The spatial discretization*

We use a staggered arrangement of the discretized dependent variables in the grid cell, see figure 2: the vertical component of velocity w is defined at the centres of the

horizontal edges, the radial and azimuthal components u and v are defined at the centres of vertical edges, and the pressure is defined at cell centres. The horizontal walls and the disk are placed on the grid lines so that w is defined on them while u and v are defined on the vertical boundaries $r = 0$ and $r = r_{max}$, but not on the horizontal ones.

The most problematic region is around the disk edge ($r = 1$, $z = 0$) since the analytical solution there has a singularity: the pressure is expected to behave like $s^{-1/2}$ and the meridional velocity components like $s^{1/2}$, where s is the distance from the edge in the (r, z)-plane. By setting one of the vertical grid lines at $r = 1$ (disk radius) we avoid the computation of pressure and velocities at this singular point (see figure 2). In other words, the disk edge is formally a grid point, but it is not a point where a discretized physical value is sought. However, the disk also provides the physical boundary conditions (2.12) for the computational cells which embed the edge. Consequently, the computations of the discretized variables near the edge can be performed as for any ordinary point near a boundary.

The justification of this formally regular treatment of the disk edge region is as follows. The staggered grid arrangement used here provides essentially a finite volume discretization. In this context, the use of the variables near the edge means that we take into account the integrated action over a cell boundary of the pressure and shear stress; we know that this action is finite, $O(s^{1/2})$, for the computational cells which embed the edge. Still, some accuracy is sacrificed due to the simplicity of this treatment of the singularity, and some additional considerations and tests were performed for further justification, as discussed later. We keep in mind that we are not interested in the details of the flow field near the edge, but rather in circumventing the difficulties posed by the singularity without loss of accuracy further away (say, 2–3 grid intervals) from the edge. The expectation for localized influence of a local relatively large error is supported by the ellipticity of the equation for the pressure, see below, by which the discretized flow field is actually computed.

For easy implementation of the boundary conditions on the vertical surfaces we use 'dummy' points for u and v, and we do the same with w on the vertical boundaries.

For the discretization of the system (2.8)–(2.11) we have to approximate the first derivatives $\partial/\partial r$ and $\partial/\partial z$ of the functions u, v, w and p and second derivatives $\partial^2/\partial r^2$ and $\partial^2/\partial z^2$ of the functions u, v and w. Since the time derivative of any velocity component is expressed by (2.8)–(2.10) through the spatial derivatives of this component only, the first and second derivatives of velocity components have to be discretized at the points of definition of these components. Such discretization is performed by means of three points (the point at which the derivative has to be approximated and its two neighbours) by the standard formulae

$$\frac{\partial f}{\partial x} \approx \frac{f_{i+1}(x_i - x_{i-1})^2 - f_{i-1}(x_{i+1} - x_i)^2 + f_i\left((x_{i+1} - x_i)^2 - (x_i - x_{i-1})^2\right)}{(x_{i+1} - x_i)(x_i - x_{i-1})(x_{i+1} - x_{i-1})} \tag{2.18}$$

and

$$\frac{\partial^2 f}{\partial x^2} \approx 2\frac{f_{i+1}(x_i - x_{i-1}) + f_{i-1}(x_{i+1} - x_i) - f_i(x_{i+1} - x_{i-1})}{(x_{i+1} - x_i)(x_i - x_{i-1})(x_{i+1} - x_{i-1})}, \tag{2.19}$$

where f stands for u, v or w and x stands for z or r. In this discretization z-derivatives are just central differences in the whole domain except the boundaries of the fine-grid regions. First derivatives always have second-order accuracy. Second derivatives in z have first-order accuracy at the boundaries of the fine-grid regions and second order

in the rest of the domain (where they are central differences) and second derivatives in r always have second-order accuracy since $(r_{i+1} - r_i) - (r_i - r_{i-1}) = O((r_i - r_{i-1})^2)$.

The discretization of pressure derivatives is coupled with the discretization of the continuity equation (2.11) and, as we shall show in § 2.4, (2.11) is not solved independently, but it is used as a basis for the derivation of the pressure equation. We discretize the derivatives for (2.11) in cell centres and use a standard central difference approximation which is second-order accurate. The pressure derivatives are also approximated by central differences and they are second-order accurate in the whole domain except the z-derivatives at the boundaries of the fine-grid regions, since there the difference is not applied in the segment centre.

For the discretization of the nonlinear terms we also have to interpolate u to grid-points where w is defined and w to points where u and v are defined. All these interpolations are performed by averaging of the four neighbouring values and this interpolation is of second-order accuracy everywhere except the interpolation of u on the boundaries of the fine-grid regions where w is defined.

A formal disadvantage of the discretization is the sharp change of the vertical grid interval on the boundary of the refined region, which leads to a local loss of accuracy, i.e. the approximations of $\partial^2/\partial z^2$, $\partial p/\partial z$ and u there have first-order accuracy. We could have avoided this problem if we had used a smooth grid, but it would complicate the process of moving planes and refining. We can argue that the effect of this non-smoothness is not significant, because it is performed well outside the Ekman layers, in regions where the flow field is expected to have a very mild dependence on z. This was indeed confirmed by comparing results obtained on several grids with different vertical intervals. Some results are presented in tables 1 and 2 for a configuration with $E = 10^{-3}$, $Ro = 10^{-2}$, $H = 1$ and the disk initially placed in the middle of the container. The comparisons were performed after 40 steps with $\Delta\mathscr{T} = \frac{1}{60}$ ($\mathscr{T}$ is time scaled with Ω^{*-1}). The grid has 60 intervals in the radial direction, and the minimal thickness of the refined region was $\frac{2}{75}$.

Tables 1 and 2 display the drag force and the radial velocity at $r = 1$, $z = 0.1333$ (at the boundary of the refined region), respectively, calculated with the non-uniform axial grids (first column) and with uniform axial grids (second column). In the first row we present results of calculations with $\Delta z_{\text{fine}} = \frac{1}{75}$ and in the second row we present results of calculations with $\Delta z_{\text{fine}} = \frac{1}{150}$. The third row shows the difference between the first two rows, i.e. the influence of changing Δz_{fine}. The third column shows the difference between the first two columns, i.e. the influence of a uniform grid. It is evident that the influence of the value of Δz_{fine} on the resolution is much more pronounced than the error associated with the use of a non-uniform grid. We conclude that it is justified to insist on a good resolution in the Ekman layers, but this does not necessitate a global smooth refinement of the grid.

The foregoing estimates of numerical accuracy do not hold in the close vicinity of the edge ($r = 1$, $z = 0$). The attempt to represent the $s^{1/2}$-like behaviour of the velocities there by a polynomial, as implied by the finite-difference method, leads to persistent errors in the viscous stress on the boundary of the numerical cells around the edge. However, although these errors may be large (say, 30%), they are local and their influence is proportional to the size of the grid intervals near the edge. We recall that these grid intervals are designed to be very small, and in particular smaller than the viscous length scale $E^{1/2}$. Heuristically, the effect of these errors can be regarded as similar to the effects of a change in the local viscosity of the fluid (in a region near the edge of the size of the computational cell) by, say, 30%. Such an effect is

Δz_{fine}	$\Delta z_{\text{main}} = \frac{1}{15}$	$\Delta z_{\text{main}} = \Delta z_{\text{fine}}$	$\delta\,(\%)$
$\frac{1}{75}$	4119.0	4117.6	0.034
$\frac{1}{150}$	4146.3	4144.8	0.036
$\delta\,(\%)$	0.66	0.66	

TABLE 1. Drag force in non-uniform and z-uniform grids with the same resolution in Ekman layers for $E = 10^{-3}$, $Ro = 10^{-2}$, $H = 1$.

Δz_{fine}	$\Delta z_{\text{main}} = \frac{1}{15}$	$\Delta z_{\text{main}} = \Delta z_{\text{fine}}$	$\delta\,(\%)$
$\frac{1}{75}$	0.2635	0.2630	0.19
$\frac{1}{150}$	0.2648	0.2643	0.19
$\delta\,(\%)$	0.49	0.49	

TABLE 2. Radial velocity at $r = 1$, $z = 0.1333$ (the boundary of the fine-grid region of non-uniform grid) in non-uniform and z-uniform grids with the same resolution in Ekman layers for $E = 10^{-3}$, $Ro = 10^{-2}$, $H = 1$.

expected to have a very mild influence on the flow field outside the corner region, and in particular on the drag force. This has been confirmed by some numerical tests as discussed later.

The drag force was calculated by two different methods, and the agreement between the results served as an additional check of the accuracy of the numerical solution. The direct way is the computation of the total force acting on the disk, as caused by the pressure difference between the upper and lower sides,

$$D = 2\pi \int_0^1 [p(r, 0+) - p(r, 0-)] r \, \mathrm{d}r. \tag{2.20}$$

Here there is no contribution from the viscous stresses to the force on the thin-disk particle because: (*a*) the normal viscous stress for $0 \leqslant r < 1$, $z = 0$ vanishes identically†, and (*b*) although the singular behaviour of the velocities, and in particular of w, introduces shear stresses $O(s^{-1/2})$ near the edge ($r = 1$, $z = 0$), the integral of these stresses over a small circle in the (r, z)-plane of radius $s = d$ around the edge is $O(d^{1/2})$ which indicates that the contribution to the force vanishes in the limit $d \to 0$.

The second method for the drag evaluation is based on the computation of the total force acting on the walls of the container. These two forces, on the particle and on the boundaries, are expected to be equal in absolute value since the total acceleration of the fluid is zero (its centre of mass does not move), and hence the total force acting on the fluid has to be zero as well. The total force acting on the container is contributed by the pressure difference between the top and the bottom walls and the viscous shear on the sidewall; therefore we obtain

$$D = 2\pi \int_0^{r_{max}} [p(r, H_u) - p(r, H_l)] r \, \mathrm{d}r - 2\pi r_{max} \int_0^{2H} \left. \frac{\partial w(r, z)}{\partial r} \right|_{r = r_{max}} \mathrm{d}z. \tag{2.21}$$

As expected, the shear term in (2.21) turns out to be negligibly small compared with the pressure term for all the short container configurations we have considered

† The azimuthal viscous stresses on the particle may, however, generate a net torque unless the boundary condition ω_p is properly defined.

No. of r-intervals:	30	50	60	100	110	120
$\Delta z_{\text{main}} = \frac{1}{15}$	26527	26558	26590	26675	26686	26698
$\Delta z_{\text{main}} = \frac{1}{30}$	26617	26655	26684	26777	26787	26801
$\Delta z_{\text{main}} = \frac{1}{60}$	26629	26675	26706	26802	26815	26827
Extrap. in z	26633	26682	26713	26810	26824	26836

TABLE 3. The drag force for $E = 10^{-3}$, $Ro = 10^{-2}$, $H = 1$ as obtained with (2.21) on different grids, at time $\mathscr{T} = 10$ with $\Delta\mathscr{T} = \frac{1}{1200}$. $\Delta z_{\text{fine}} = \Delta z_{\text{main}}/5$. The last row gives extrapolated values using $\Delta z_{\text{main}} = \frac{1}{30}$ and $\frac{1}{60}$. When (2.20) is used the last row (extrapolated values) is 26639, 26684, 26716, 26811, 26827 and 26837.

in this study. The use of the reduced pressure instead of the physical one for the computation of the drag force requires a straightforward correction to (2.21) when z accelerations are present. In the present study the agreement between the two different computations of the drag force was within 1%. The good agreement between the results obtained via the two different methods for the drag evaluation, as discussed below, provides additional confirmation of the validity of (2.20).

We emphasize that the direct evaluation of the drag force points out the formal difficulty associated with this variable. The analytically predicted $O(s^{-1/2})$ singularity of the pressure at the edge of the disk indicates that a large truncation error in the result of (2.20) cannot be *a priori* excluded. However, such an error did not appear in our computations. Since the pressure is calculated at the middle of the computational cells, the integral of the pressure is essentially performed by the rectangle (or midpoint) method, which is able to approximate straightforwardly integrals of the form $\int_0^b s^{-1/2}\,\mathrm{d}s$ (the rate of convergence is low, only $\frac{1}{2}$, but nevertheless with three points in the interval $(0, b)$ the error is already less than 20%). Moreover, Vedensky & Ungarish (1994) estimated analytically that the contribution of this singularity to the drag force is relatively small, which means that a high numerical resolution of the singularity region is not necessary for obtaining an accurate result for the global drag force. Our estimate of the mild contribution of the singularity to the numerical error was systematically confirmed by comparisons discussed below between (*a*) numerical results on different grids, and (*b*) exact linear results, which take this singularity into account, and the corresponding numerical results with $Ro = 10^{-4}$, which were obtained without taking any special measures to deal with the singularity.

Consider the influence of the grid size (i.e. the spatial truncation errors) on the accuracy of the drag force result. We illustrate this feature for the typical configuration with $E = 10^{-3}$, $Ro = 10^{-2}$, $H = 1$, and the disk initially placed in the middle of the container. The drag force obtained at $\mathscr{T} = 10$ (at about $\frac{1}{3}$ of the spin-up time interval) with $\Delta\mathscr{T} = \frac{1}{1200}$, on different grids, is displayed in table 3. In this table each row corresponds to a constant value of Δz_{main} and each column corresponds to a constant number of radial grid intervals. In each case $\Delta z_{\text{fine}} = \Delta z_{\text{main}}/5$. The associated table 4 presents the deviations of the results from the value obtained with the largest number of computational points. We mention that this grid contains about 9×10 intervals in the $E^{1/2} \times E^{1/2}$ corner region near the disk edge; the coarsest grid has about 2×3 intervals in this region.

The results converge monotonically as the numbers of both radial and axial grid

r-intervals	30	50	60	100	110	120
$\Delta z_{\text{main}} = \frac{1}{15}$	−1.12	−1.00	−0.88	−0.57	−0.53	−0.48
$\Delta z_{\text{main}} = \frac{1}{30}$	−0.78	−0.64	−0.53	−0.19	−0.15	−0.10
$\Delta z_{\text{main}} = \frac{1}{60}$	−0.74	−0.57	−0.45	−0.09	−0.04	0.00

TABLE 4. The *percent* relative deviation of D from the value $D = 26827$ obtained on the finest grid of table 3.

intervals increase. The difference between the results on the coarsest grid and on the finest grid is only about 1%. This indicates that when the minimal axial and radial intervals are both less than about $0.5E^{1/2}$ acceptable accuracies, of about 1%, are expected.

We inspected carefully the rate of convergence of these results. The axial dependence indicated a second-order accuracy, as expected, and accordingly we performed one step of Richardson extrapolation.† The outcomes are also presented in table 3. The radial order of convergence is less evident. The second-order accuracy is lost because of the singularity at the edge $r = 1$, but the observed convergence is faster than the $\frac{1}{2}$ order expected for the rectangle rule quadrature discussed above. We used the empirically estimated $\frac{3}{4}$ order of convergence for extrapolating in the radial direction the z-extrapolated values for 100 and 120 radial intervals. The result of this double extrapolation is $D = 27013$, which is 0.7% larger than the result of the 'best' grid and 1.8% larger than the result of the 'worst' grid.

We conclude these inspections and estimates of the behaviour of errors on different grids that, in spite of our meagre treatment of the edge singularity, accuracies of about 1% are attainable in the range of parameters of interest within a moderate number of grid intervals. This provides support for our expectation that the singularity has a local and minor influence on the numerical results and validates the method by which we circumvented the associated difficulties. Both ways of drag calculation, by (2.20) and (2.21), lead to the same conclusions.

We would like to mention, without going into details, that additional numerical tests were carried out to strengthen our confidence in our conclusion about the localized influence of errors incurred by the discretization near the edge. These included (*a*) the inspection of the velocity and pressure fields and of the different terms in the momentum equations near the edge on various grids; and (*b*) computations with intentionally perturbed values of the parameters E and Ro in the vicinity of the edge (which emulate non-vanishing local truncation errors). All the tests indicated that the edge perturbations decay in the $E^{1/2} \times E^{1/2}$ corner and the residual effect, if any, was usually in the fourth digit of the inspected variables. The comparison of the numerical results with analytical solutions, which is discussed below, provides further support for our confidence on this matter.

2.4. *The Poisson equation for pressure*

For each time step the advance from the known velocity field $\boldsymbol{v}^n$ to the new field $\boldsymbol{v}^{n+1}$ is performed in two stages. In the first stage we consider explicitly, via the momentum equations, the contribution of viscous, Coriolis and inertial terms to the change of

† Schematically, $A = (A_2 - q^p A_1)/(1 - q^p)$ where q is the interval ratio of grid 1 to grid 2 and p is the asymptotical order of convergence.

velocity during the time step, and obtain a first approximation, denoted $\tilde{\boldsymbol{v}}^{n+1}$, as follows:

$$\tilde{u}^{n+1} = u^n + \frac{\Delta t}{Ro}\left[E\left(\frac{\partial^2 u^n}{\partial r^2} + \frac{1}{r}\frac{\partial u^n}{\partial r} + \frac{\partial^2 u^n}{\partial z^2} - \frac{u^n}{r^2}\right) + 2v^n - Ro\left(u^n\frac{\partial u^n}{\partial r} - \frac{v^{n2}}{r} + w^n\frac{\partial u^n}{\partial z}\right)\right],$$

$$\tilde{v}^{n+1} = v^n + \frac{\Delta t}{Ro}\left[E\left(\frac{\partial^2 v^n}{\partial r^2} + \frac{1}{r}\frac{\partial v^n}{\partial r} + \frac{\partial^2 v^n}{\partial z^2} - \frac{v^n}{r^2}\right) - 2u^n - Ro\left(u^n\frac{\partial v^n}{\partial r} + \frac{u^n v^n}{r} + w^n\frac{\partial v^n}{\partial z}\right)\right],$$

$$\tilde{w}^{n+1} = w^n + \frac{\Delta t}{Ro}\left[E\left(\frac{\partial^2 w^n}{\partial r^2} + \frac{1}{r}\frac{\partial w^n}{\partial r} + \frac{\partial^2 w^n}{\partial z^2}\right) - Ro\left(u^n\frac{\partial w^n}{\partial r} + w^n\frac{\partial w^n}{\partial z}\right)\right],$$

where the spatial derivatives are approximated with the use of (2.18) and (2.19). This intermediary flow field is, of course, not expected to satisfy the equation of continuity.

In the next stage, we incorporate the contribution of the as yet unknown pressure field, p^{n+1}, and subject it to the condition that the new velocity field has to satisfy the continuity equation (2.11). A detailed discussion of the emergence of the Poisson pressure equation in the time-marching solution of the Navier–Stokes equations is given by Karniadakis *et al.* (1991). For formulating a discrete equation for the pressure we have to discretize (2.11). Denoting the cell centre's coordinates by r_i, z_j, we refer to velocities in the surrounding points as $u_{i-1/2,j}$, $u_{i+1/2,j}$ and $w_{i,j-1/2}$, $w_{i,j+1/2}$ (see figure 2). The discrete analogue of (2.11) on the $(n+1)$th time step is

$$\frac{1}{r_i}\frac{u^{n+1}_{i+1/2,j}r_{i+1/2} - u^{n+1}_{i-1/2,j}r_{i-1/2}}{r_{i+1/2} - r_{i-1/2}} + \frac{w^{n+1}_{i,j+1/2} - w^{n+1}_{i,j-1/2}}{z_{j+1/2} - z_{j-1/2}} = 0. \tag{2.22}$$

Taking into account that

$$u^{n+1}_{i-1/2,j} = \tilde{u}^{n+1}_{i-1/2,j} + \Delta t\frac{p^{n+1}_{i,j} - p^{n+1}_{i-1,j}}{r_i - r_{i-1}},$$

$$u^{n+1}_{i+1/2,j} = \tilde{u}^{n+1}_{i+1/2,j} + \Delta t\frac{p^{n+1}_{i+1,j} - p^{n+1}_{i,j}}{r_{i+1} - r_i},$$

$$w^{n+1}_{i,j-1/2} = \tilde{w}^{n+1}_{i,j-1/2} + \Delta t\frac{p^{n+1}_{i,j-1} - p^{n+1}_{i,j}}{z_{j-1} - z_j},$$

$$w^{n+1}_{i,j+1/2} = \tilde{w}^{n+1}_{i,j+1/2} + \Delta t\frac{p^{n+1}_{i,j+1} - p^{n+1}_{i,j}}{z_{j+1} - z_j},$$

we obtain after simple manipulations

$$\frac{2\Delta t}{z_{j+1}-z_{j-1}}\left[\frac{p^{n+1}_{i,j+1}}{z_{j+1}-z_j}+\frac{p^{n+1}_{i,j-1}}{z_j-z_{j-1}}-p^{n+1}_{i,j}\left(\frac{1}{z_{j+1}-z_j}+\frac{1}{z_j-z_{j-1}}\right)\right]$$

$$+\frac{2\Delta t}{r_{i+1}-r_{i-1}}\left[\frac{p^{n+1}_{i+1,j}r_{i+1/2}}{r_{i+1}-r_i}+\frac{p^{n+1}_{i-1,j}r_{i-1/2}}{r_i-r_{i-1}}-p^{n+1}_{i,j}\left(\frac{r_{i+1/2}}{r_{i+1}-r_i}+\frac{r_{i-1/2}}{r_i-r_{i-1}}\right)\right]$$

$$=\frac{1}{r_i}\frac{\tilde{u}^{n+1}_{i+1/2,j}r_{i+1/2}-\tilde{u}^{n+1}_{i-1/2,j}r_{i-1/2}}{r_{i+1/2}-r_{i-1/2}}+\frac{\tilde{w}^{n+1}_{i,j+1/2}-\tilde{w}^{n+1}_{i,j-1/2}}{z_{j+1/2}-z_{j-1/2}},$$

which is a discrete Poisson equation for p^{n+1}. The boundary conditions are of Neumann type and provided by the radial and axial momentum equations evaluated at the boundary of the computational domain while accounting for the boundary conditions of the velocity; the resulting values are implemented with the aid of dummy points outside the boundary. The arbitrary constant difficulty associated with the Neumann condition is fixed by prescribing the value of p at one grid point near the disk.

The solution of the Poisson equation for the pressure is performed by the SOR method. The maximal absolute value of the difference between two successive iterations is used as a convergence criterion, and the process is stopped when this difference decreases below some value ϵ, typically about 10^{-7}, which by inspection was fixed small enough so that further decrease had no effect on the flow field. The weak dependence of the pressure on the z-coordinate makes the block-SOR method with radial-directed blocks efficient. In fact, this block-SOR method improves convergence significantly in certain configurations (long container) but is not effective in others; the gain in convergence speed may be lost by the additional computation needed for one iteration. In both cases (using the regular or blocked-SOR method) we used an over-relaxation parameter α smaller than the 'optimal' one. We find 'experimentally' that every configuration has its own optimal α which minimizes the eigenvalues which correspond to the local changes in pressure. We do this by measuring the SOR convergence rate after the formation of the Ekman layers when the changes in the pressure field become local, and not at the initial time steps.

2.5. *Validation of the numerical results*

As previously mentioned, the controlled variation of the computational parameters like the grid steps and time steps and the convergence criterion ϵ of the solution of the pressure equation has small and continuous effects on the solution, and indicates that the present numerical solution converges to acceptable accuracy for practical values of the grid interval and time step.

We consider 'acceptable accuracy' in the present study as containing errors of up to about 1% in the value of the drag force and angular velocity in the core and up to about 3% in the value of the meridional stream function (with possible local exceptions in regions of small velocity). The reason is that the effects we wish to understand can be safely detected and analysed within this range of accuracy. For instance, the drag discrepancies between the geostrophic theory and the experiments of Maxworthy (1968) were about 20% while the experimental errors were about 2%; it is actually very unlikely that drag force measurements with a higher accuracy will be available in the next decade. The discrepancies between the geostrophic, quasi-geostrophic and full analytic-linear results in the range of parameters of this investigation are also typically larger than 10%. The effects of asymmetrical position, nonlinear terms and

time-dependence which are considered below cause quite significant variation from the 'basic' flow field which can be readily recognized even if the abovementioned errors are present.

To assess the physical validity of the numerical results it is of course desirable to also verify the compatibility of the present computations with physically acceptable solutions obtained by different, preferably analytical, methods; and we performed such comparisons. The most significant candidates for comparison, for the disk-particle configuration, are the results of Ungarish & Vedensky (1995). These results were obtained by an analytical transform method and can be considered essentially 'exact' from a mathematical point of view, but they cover only the special linear case $Ro = 0$, and a very particular configuration: the (quasi) steady flow with the disk in a strictly symmetric position between the plates, and, moreover, in a radially unbounded fluid ($r_{max} \to \infty$). These conditions, obviously, cannot be exactly reproduced with the numerical code. We used instead $Ro = 10^{-4}$ and $2 \leqslant r_{max} \leqslant 5$ (depending on the values of E and H). Some of these comparisons are presented in this paper, and other will be described in a sequel paper on the long container configuration (Part 2). Almost all comparisons concern small Ekman number (large Taylor number) cases, which are expected to represent the more difficult parametric range from the computational point of view. In the long container case comparisons were also performed at $E = 1$. In all the tested cases excellent agreement was obtained. Unfortunately, no independent solutions for the nonlinear (finite values of Ro) cases are available for a reliable quantitative comparison.

In most of the computations the time step was chosen due to stability requirements, but in any case we have assessed the resulting accuracy by repeating computations with different time steps. Similar checks were performed for the chosen grid parameters: the number of vertical and horizontal grid intervals, the number of refined vertical intervals, r_{max}, etc. The typical grid size is about 150 radial intervals and 100–400 vertical intervals. The number of time steps may vary from 10 000 to 300 000. The computations were carried out in double-precision on a DEC/AXE alpha 8800-5/300 (of which only one CPU was used) computer. The total CPU time for one run varied from about one hour for a short container configuration to about 50 hours for a long container configuration. More than 80% of the CPU time was dedicated to the solution of the Poisson equation for the pressure in the long container configuration; for the short container this task took more than 90% of the CPU time.

3. The developed flow ('steady state')

Here we discuss the flow field obtained several spin-up time intervals after start from rest, $t > 2HRoE^{-1/2}$ (the time-dependent motion will be discussed later). If not stated otherwise, the particle is in the middle of the container (approximately, with a possible dimensionless deviation $O(Ro)$ due to the motion).

3.1. *Linear flow limit*

For $Ro = 0$ the equations of motion (2.8)–(2.11) become linear and time-independent. The analytical solution of these equations has been obtained by Ungarish & Vedensky (1995) and is the most obvious item for comparison with the present solution at a small value of Ro. We start with the pattern of the stream function for $E = \frac{1}{6400}$ and different values of H, and present side by side contour lines from Ungarish & Vedensky (1995, figure 5) and the present ones obtained for $Ro = 10^{-4}$.

Only the upper region is shown and discussed because of symmetry with respect to

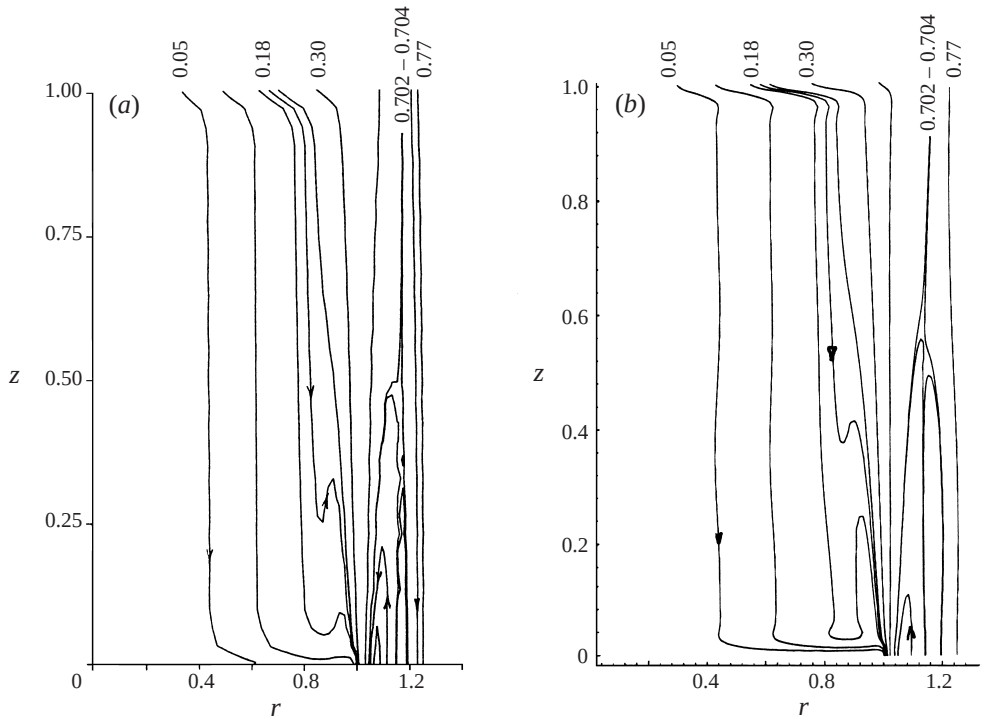

FIGURE 4. The contour lines of the stream function for $E = \frac{1}{6400}$, $H = 1$. Analytical (*a*) and numerical (*b*) results. The computation was performed on a 60×170 grid with 15000 time steps and $Ro = 10^{-4}$.

$z = 0$. The flow field displays the classical structure and behaviour: the plate above the rising disk pushes fluid into the upper Ekman layers, where it moves outward, and likewise the disk pushes fluid into the lower Ekman layer where it also moves outward. In the core there is no radial motion of the fluid. Close to $r = 1$ the $E^{1/4}$ shear layer assists the Ekman layers in the radial transport of the fluid, which is next transported by the $E^{1/3}$ layer to and around the edge of the disk to the lower region. The $E^{1/3}$ layer extends well into the $r > 1$ domain, where a recirculation appears. Note that according to our definition the value of ψ is zero on the axis and on the disk, while on the solid walls $\psi = 0.5r^2$.

Figure 4 shows the $H = 1$ configuration. The numerical and analytical results are in very good agreement. There is a difference in the Ekman layer domains which can be attributed to the low resolution of the plotting method used for the analytical solution. For a good representation of the Ekman layer several points are needed in the axial interval $E^{1/2} = \frac{1}{80}$. The distance between the sample points in the figure for the numerical stream function is $\frac{1}{200}$ and therefore a good graphical presentation is possible, and indeed the shape of the Ekman layers in the numerical plot is the classical one and includes a region with negative radial velocity. On the other hand, in the graph of the analytical stream function the interval between the sample points is about $\frac{1}{30}$, and details are obscured; however, this is only a drawback of the representation, not of the analytical result itself.

The flow-field details outside the Ekman layers agree very well. Note that the recirculation in the inner Stewartson layer is a delicate feature because of its connection with the disk edge and its sandwiched position between the $E^{1/4}$ layers. In

both solutions the recirculation occurs between the stream lines with values 0.702 and 0.704. The length and the thickness of the recirculation region, and the value of the maximal stream line (0.77) are also very close for the compared graphs.

For longer cylinders, as H was increased to 2 and 4 (see Minkov 1998) the same agreement between the analytical and numerical results was observed. The sandwich region of the Stewartson layers becomes thicker as H increases, and the lower bound of the stream function in the recirculation region also increases. These changes show up in the same qualitative and quantitative manner in both the analytical and numerical results. The small discrepancies between the analytical and numerical results in the tested configurations can be attributed to the resolution of the plot and truncation errors (in both the numerical and 'analytical' values of ψ).†

Of major interest is the drag force agreement between the analytical and numerical solutions. The comparison involves several approaches: (*a*) the geostrophic drag, D_0, obtained by assuming that the flow is composed of inviscid cores and Ekman layers (no contribution from the vertical Stewartson layers), following Moore & Saffman (1968), is used for scaling; (*b*) the quasi-geostrophic drag ($D_{\mathrm{q-g}}$) derived by Ungarish (1996) by incorporating the effects of Ekman and outer Stewartson layers (but no contribution from the vertical $E^{1/3}$ Stewartson layer); (*c*) analytical-linear drag, $D_{\mathrm{a-l}}$, computed by Ungarish & Vedensky via a solution of the full linear equations; and (*d*) numerical results (D_{num}).

The results of the geostrophic approximations are simply

$$\omega_u = -\omega_l = \begin{cases} -\frac{1}{2}E^{-1/2} & (0 < r < 1) \\ 0 & (r \geqslant 1), \end{cases} \tag{3.23}$$

$$D_0 = \frac{\pi}{2}E^{-3/2}, \tag{3.24}$$

and results of the quasi-geostrophic approximations (in the symmetrical case) are

$$\omega_u = -\omega_l = \begin{cases} -\frac{1}{2}E^{-1/2}\left[1 - \dfrac{I_1(r/\varepsilon)}{rI_1(1/\varepsilon)}\right] & (0 < r \leqslant 1) \\ 0 & (r \geqslant 1), \end{cases} \tag{3.25}$$

$$D = \frac{\pi}{2}E^{-3/2}\left[1 - 4\varepsilon\frac{I_2(1/\varepsilon)}{I_1(1/\varepsilon)}\right], \tag{3.26}$$

where I_j are the modified Bessel functions and $\varepsilon = (H/2)^{1/2}E^{1/4}$ is the length scale of the $E^{1/4}$ vertical shear layer. The values of ω_u and ω_l are for the upper and lower cores outside the Ekman layers. In both geostrophic and quasi-geostrophic models there is a strong connection between the angular velocity and the drag: both use the geostrophic radial momentum equation $2\omega r = E\partial p/\partial r$ for obtaining p and then employ (2.20).

The full analytical-linear results cannot be expressed in simple closed form formulae.

We observe briefly that the geostrophic results which discard the presence of the vertical Stewartson layers, both of $E^{1/4}$ and of $E^{1/3}$ type, contain discontinuities of ω at $r = 1$. The quasi-geostrophic results smooth out the discontinuity of ω in the $E^{1/4}$ Stewartson layers; indeed, for small ε the relative difference between (3.25) and (3.23) is $\exp[-(1-r)/\varepsilon]$for $r < 1$. In general, when $H_u \neq H_l$, there is also an $E^{1/4}$

† We keep in mind that the contour lines were calculated and plotted by commercial software which uses various two-dimensional interpolation and smoothing methods for processing the tables of values and coordinates.

E	H	D_{q-g}/D_0	D_{a-l}/D_0	D_{num}/D_0
10^{-3}	1	0.59	0.91	0.90
	5	0.30	0.62	0.62
	8	0.22	0.53	0.52
10^{-4}	0.5	0.81	0.94	0.93
	1	0.75	0.90	0.88
	5	0.51	0.69	0.68
	8	0.43	0.61	0.60

TABLE 5. Drag force computed by quasi-geostrophic model, analytic-linear model and numerically for $Ro = 10^{-4}$ scaled by the geostrophic value.

Stewartson layer for $r > 1$. In the $E^{1/4}$ Stewartson layers ω (as well as u and p) is z-independent.† The quasi-geostrophic results do not satisfy in detail the continuity of $\partial\omega/\partial r$ at $r = 1$. These (and other flow-field adjustments) occur in a shear layer of thickness $(HE)^{1/3}$ (the $E^{1/3}$ Stewartson layer) which is 'sandwiched' between $E^{1/4}$ layers. The adjustment of the shear induces the recirculation discussed above. Both the geostrophic and the quasi-geostrophic approximations require a small value of $E^{1/2}$, which is readily attainable in experiments. However, for accuracy of (3.24) a small value of $\varepsilon = (H/2)^{1/2}E^{1/4}$ is needed, and for accuracy of (3.26) a small value of $(HE)^{1/3}$ is necessary. The full analytical-linear solution does not rely on boundary layer matching methods and therefore its accuracy is formally unrestricted by the values of these parameters (however, errors estimated as about 1% are introduced by various truncations needed in the practical computations).

Typical drag force results are presented in table 5. The analytical values used in table 5 are taken from table 1 of Ungarish & Vedensky and the numerical drag force was computed for $Ro = 10^{-4}$. The table shows that the numerical results are very close to the full analytical-linear ones (the differences between them are of order 1%). The quasi-geostrophic results, although providing the correct trends when E and H vary, are significantly below the numerical results. (The numerical drag force is in some cases slightly below the analytical value; however, we note that the results of table 3 indicate a slight increase of drag force when the numerical resolution is improved. This suggest that an improved numerical resolution would yield an even better agreement between D_{num} and D_{a-l}.)

The excellent agreement between the present numerical solution of the full Navier–Stokes equations and the analytical solution of the linear steady-state equations has several implications. First, it gives credence to both the analytical solution and to the numerical approach and its accuracy. We recall that in the process of calculating the analytical results (which are actually given as infinite series involving integrals with Bessel functions kernels over semi-infinite domains) it was necessary to make some simplifications to avoid cancellation errors, and, in addition various truncation errors were introduced, which made an independent verification quite desirable. Second, it clearly indicates that the linear theory results are a regular limit of the solutions of the Navier–Stokes equations for small Ro. In other words, results and conclusions derived for the non-physical case of $Ro = 0$ (strictly speaking, when no motion takes

† For a spherical particle the $E^{1/4}$-type shear layers perform a different matching task, but the flow field and in particular the influence on the drag force are similar to the disk geometry. For details see Moore & Saffman (1968) and Ungarish (1996).

place) are relevant to real cases of slow motion with small but still practical values of the Rossby number. However, this conclusion is of less practical importance than could be anticipated: although the linear equations are much simpler than the full Navier–Stokes system, obtaining their solution for the rising body problem in a top and bottom bounded domain is still a formidable task, which so far has been carried out only for a disk particle at midplane position (Ungarish & Vedensky 1995). The approximate solutions of the linear equations, termed the geostrophic model and the quasi-geostrophic model, can be obtained with little computational effort, but yield significant errors in the predicted drag.

The reason for these discrepancies has been shown to be the omission of the vertical shear layers in the geostrophic model and the omission of the $E^{1/3}$ shear layer in the quasi-geostrophic model. The magnitude of the influence of the thin $E^{1/3}$ layer is surprising (e.g. a 15% contribution for $E = 10^{-4}$, $H = 1$ and a 52% contribution for $E = 10^{-3}$, $H = 5$ case, respectively). The present numerical solution allows some further clarification of the role played by the $E^{1/3}$ layer in the determination of the drag force, and hence in the disagreement between the quasi-geostrophic approximate result and the correct drag force, as follows.

The quasi-geostrophic model (Ungarish 1996) predicts that the radial momentum equation is well approximated by the z-independent Coriolis–pressure balance,

$$-2v = -E\frac{\mathrm{d}p}{\mathrm{d}r}, \tag{3.27}$$

everywhere except for the Ekman layers. Under this approximation we can calculate the drag force by

$$D = 2\pi \int_0^1 [p(r, z_u) - p(r, z_l)] r \, \mathrm{d}r, \tag{3.28}$$

where z_u is some axial position in the upper core and z_l in the lower core (it has been confirmed by the numerical results that p is z independent outside the Ekman layers; this holds, to fair accuracy, even in the $E^{1/3}$ layer.) Next, using the connection (3.27) between the azimuthal velocity and the pressure, we obtain

$$D = 2\pi \left\{ -E^{-1} \int_0^1 [\omega(r, z_u) - \omega(r, z_l)] r^3 \, \mathrm{d}r + \tfrac{1}{2} [p(1, z_u) - p(1, z_l)] \right\}. \tag{3.29}$$

The pressure difference at $r = 1$ which appears in the last equation also can be expressed in terms of the the angular velocities in the core. Suppose that $r = r_{out}$ is some large radius, beyond the external Stewartson layer, where no fluid flow occurs. Using (3.27) we find

$$p(1, z_u) - p(1, z_l) = -2E^{-1} \int_1^{r_{out}} [\omega(r, z_u) - \omega(r, z_l)] r \, \mathrm{d}r. \tag{3.30}$$

Note that the integration can be performed at any pair of axial positions in the upper and lower cores (outside the Ekman layers). Equations (3.29) and (3.30) are expected to hold for general configurations, and simplifications are possible when symmetry with respect to the disk is present.

In the symmetric case, we can choose two symmetric planes (with respect to the disk) $z_l = -z_u$ and, using the symmetry of the flow, $\omega(r, z_l) = -\omega(r, z_u)$ for $Ro = 0$ we conclude

$$D = -4\pi E^{-1} \left[\int_0^1 \omega(r, z_u) r^3 \, \mathrm{d}r + \int_1^{r_{out}} \omega(r, z_u) r \, \mathrm{d}r \right]. \tag{3.31}$$

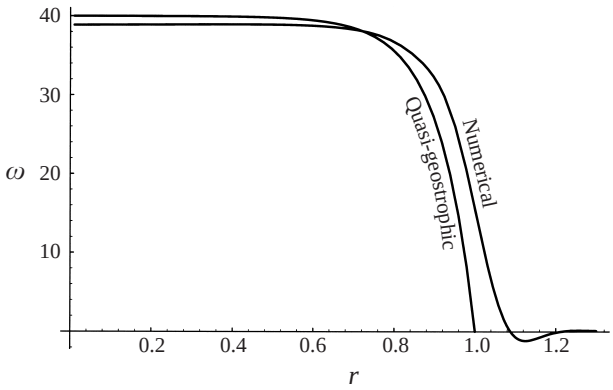

FIGURE 5. The angular velocity as a function of r for $E = \frac{1}{6400}$, $H = 1$. Quasi-geostrophic and numerical ($\pm\omega$ at $z = \mp 0.5$, $Ro = 10^{-4}$) results.

This result, although based on the approximation (3.27) for the pressure, turns out to be very accurate when compared with the present numerical calculations of the drag force. (The result of the approximation (3.31) depends, of course, on the choice of the z_u, but this dependence is quite weak.) For example, for the configuration $E = \frac{1}{6400}$, $H = 1$, $Ro = 10^{-4}$, depicted in figure 4, the drag force approximated by (3.31) differs from the directly computed value by less than 1% (for all z_u well outside the Ekman layers).

On the other hand, the drag force in the quasi-geostrophic model was calculated by

$$D_{\mathrm{q-g}} = 4\pi E^{-1} \int_0^1 |\omega_{\mathrm{q-g}}(r)| r^3 \, \mathrm{d}r \tag{3.32}$$

(Ungarish 1996, Equation (20)). There are two major contributions to the difference in the results from (3.32) and (3.31). First, the value of $\omega_{\mathrm{q-g}}(r)$ in the region $r = 1^-$ in the quasi-geostrophic model is close to zero, a consequence of an $E^{1/3}$ layer of zero thickness, and hence the contribution to the drag from this region is very small. However, the presence of an $E^{1/3}$ layer of finite thickness keeps $|\omega|$ well above 0 for $r \leqslant 1$. According to the foregoing formulae for the drag the contributions of small differences in $\omega(r)$ in the region $r \approx 1$ are amplified in the final result. We illustrate this for the case $E = \frac{1}{6400}$, $H = 1$ by comparison of the quasi-geostrophic results with a numerical computation ($Ro = 10^{-4}$). Figure 5 shows the graph of $\omega(r)$ below the disk halfway between the disk and the lower plane in the quasi-geostrophic model and in our computation. It is clearly seen that the profiles of ω are very close to each other, but the major difference occurs in the region $r \approx 1$ which is most significant for the drag. The integral of $|\omega(r)|r^3$ with respect to r from 0 to 1 is smaller by about 12% for the quasi-geostrophic approximation than for the numerical results. Thus, this difference can account for a quasi-geostrophic drag force being about 12% lower than the correct one.

Second, the quasi-geostrophic model assumes that $\omega \equiv 0$ for $r \geqslant 1$, which is again a consequence of an $E^{1/3}$ layer of zero thickness, and hence the second integral in (3.31) is predicted to vanish. This term represents the difference between the pressure above the disk and below it at $r = 1$. This pressure difference, see also (3.30), is supported by the strong viscous shear in the $E^{1/3}$ layer near the edge of the disk.

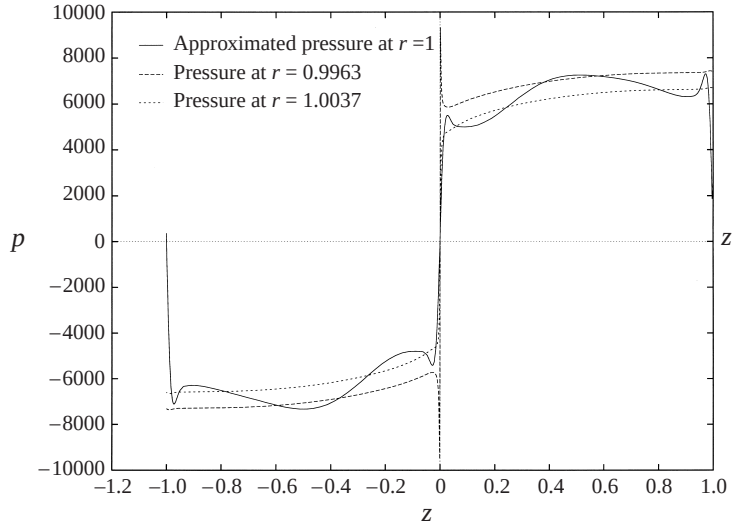

FIGURE 6. Pressure around $r = 1$ as a function of z for $E = \frac{1}{6400}$, $H = 1$, $Ro = 10^{-4}$.

In a real situation, the pressure in the upper region is expected to be higher than in the lower region to provide the driving force necessary for the volume transfer from the upper side to the lower one during the motion of the disk. Figure 6 shows, for $E = \frac{1}{6400}$, $H = 1$, the pressure as a function of z in the region $r = 1$, as obtained by direct numerical calculations at the closest grid lines (in the staggered grid p is not computed at $r = 1$), and also as estimated from (3.30) with the aid of numerically computed values of ω (this approximation cannot be applied to the Ekman viscous regions, and hence the results close to the boundaries are not expected to be correct).

These computations show that the effect of the pressure difference at $r = 1$ between the upper and lower cores, either by direct incorporation in (3.29) or by approximate incorporation by the second integral in (3.31), contributes about 6% of the drag force in the described configuration. We conclude that both contributions of the $E^{1/3}$ layer are to increase of the drag above the quasi-geostrophic value, which in the present example constitutes about 18% of the correct result.

The numerical results support the explanation of Ungarish & Vedensky (1995) and Ungarish (1996) for the discrepancy of Moore & Saffman's (1968) and Maxworthy's (1968) results for the drag force. The comparison between the angular velocity obtained from the numerical solution and quasi-geostrophic model shows that the quasi-geostrophic approximation is qualitatively accurate, but the $E^{1/3}$ layer has an important quantitative effect on the drag force as speculated by Ungarish (1996).

3.2. *Non-symmetric configurations*

The full linear equations in a top and bottom bounded domain have been solved only for the symmetrical case, $H_u = H_l = H$. (An extension of the exact solution of Ungarish & Vedensky (1995) to non-symmetric cases seems possible but is not straightforward. Davis & Stone (1998) solved the asymmetric case of a disk in a domain with a top boundary and infinite lower region which is not relevant to the short container configuration.) The geostrophic approximation for the drag force is independent of the axial positions of the particle. Ungarish & Vedensky (1995) and Ungarish (1996) by using the quasi-geostrophic model, estimated the influence of this

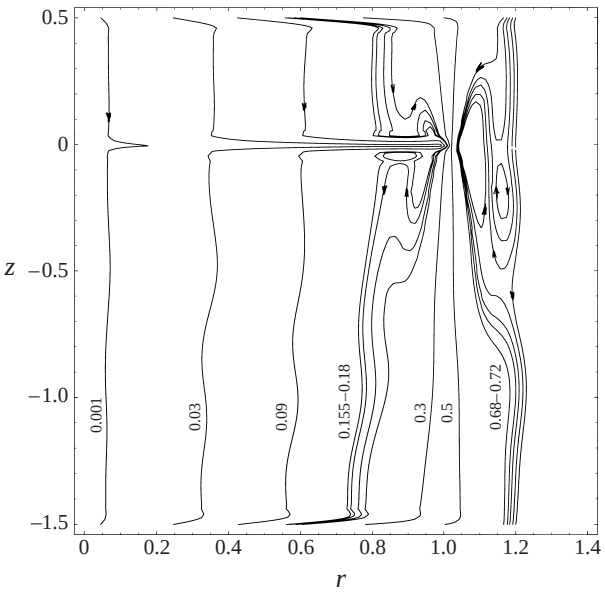

FIGURE 7. The contour lines of the stream function for $E = \frac{1}{6400}$, $H = 1$, $H_u/H = 0.5$, $Ro = 10^{-4}$.

parameter as follows: as the asymmetry increases, the drag increases monotonically but by a small amount, and the particle acquires a small (compared to the value in the core, $0.5E^{-1/2}$) angular velocity, ω_p, which is positive when $H_l < H_u$ and vice versa. Here we present some numerical results for such configurations.

Figure 7 displays the stream function for a typical asymmetric linear case $H_u/H = 0.5$ with $H = 1$ and $E = \frac{1}{6400}$. The Ekman layer and core flow are as in the symmetric case. The influence of the asymmetry is observed in the Stewartson shear layers: the $E^{1/4}$ layer in the longer region becomes slightly thicker than in the shorter region, and the region of recirculation in the $E^{1/3}$ layer becomes shorter than in the symmetric case. As expected, the corresponding $H_u/H = 1.5$ case yields a mirror image of figure 7, not shown here.

For $E = \frac{1}{6400}$, $Ro = 10^{-4}$ the numerically computed drag increased above the symmetric value by 0.26% when $H_u/H = 0.5$ and by 0.20% when $H_u/H = 1.5$, while the scaled angular velocity of the disk $\omega_p/(0.5E^{-1/2})$ changed from zero to -0.12 and 0.10, respectively. (Theoretically the absolute values of these variations should be equal for $H_u/H = 0.5$ and $H_u/H = 1.5$ in the linear case, but since we deal here with relatively small quantities the discretization errors can easily explain the inconsistencies with the expectations.)

The typical influence of the asymmetry on the angular velocity profile can be inferred from figure 8, which displays the profiles $\omega(r)$ at constant z positions above and below the disk in the configuration with $H_u/H = 0.5$. It is again evident that the $E^{1/4}$ and $E^{1/3}$ Stewartson layers are thicker on the lower side (where $H_l > H$) than on the upper side (where $H_u < H$). Due to the asymmetry, the value of $|\omega|$ increases in the upper core (by approximately $0.5|\omega_p|$) and decreases in the lower core (by the same amount), but the difference $|\omega_u - \omega_l|$, which contributes to the drag force, remains as in the symmetric case, cf. figure 5. This confirms the predictions of the quasi-geostrophic model.

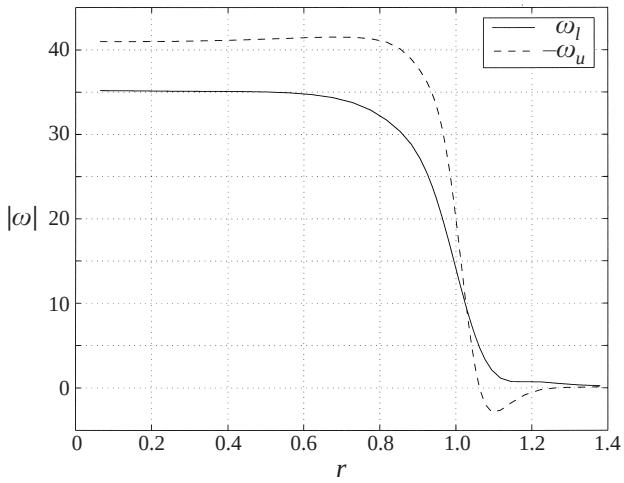

FIGURE 8. The angular velocity as a function of r for $E = \frac{1}{6400}$, $H_u/H = 0.5$, $Ro = 10^{-4}$: ω at $z = 0.25$ full line and $-\omega$ at $z = -0.75$ dashed line.

3.3. *Effect of nonlinear terms*

The classical asymptotic studies of the problem (in particular Moore & Saffman 1968) and the exact solution of Ungarish & Vedensky (1995) were concerned only with the linear flow ($Ro = 0$). Estimates by Moore & Saffman (1968) of the neglected nonlinear terms placed restrictions on the applicability of the linear theory of the form $RoE^aH^b \ll 1$, where a and b are negative constants; for a disk the restriction is $RoE^{-3/4}H^{-1/2} \ll 1$. (The parameter that reflects accurately the relative deviation of the nonlinear results from the linear theory prediction is regarded as the 'effective Rossby number', while Ro is the formal Rossby number.) However, the linear studies were unable to indicate the magnitude and even the sign of the possible contribution of the nonlinear terms to the drag and other properties. Some fallacies appeared and were accepted for many years, like Maxworthy's (1968) suggestion that the nonlinear terms are responsible for the discrepancy between the geostrophic theory and experimental observations at $E \approx 10^{-4}$ even for $Ro = 10^{-3}$ (the measured drag was about 20% lower). Ungarish & Vedensky (1995) claimed that this discrepancy has to be attributed mainly to the shear effects in the Stewartson layers, whose incorporation is indeed able to narrow the gap between the analytical linear solution and the experimental observations, but, again, an analysis of the nonlinear effects was not provided. Ungarish (1996) investigated the influence of small nonlinearities on the flow field and on the drag force by incorporating approximately the leading momentum convection terms in the quasi-geostrophic model. His results can be summarized as follows. (*a*) The major perturbations caused by the inertial terms are: a reduction of the dimensionless drag,† a negative rotation of the disk and a contraction/expansion of the upper/lower $E^{1/4}$ layer. (*b*) The linear theory, for the range of parameters E and H relevant to the experiments of Maxworthy, is

† Some care is needed in the interpretation of the influence of $Ro = W^*/\Omega^* a^*$ on the drag force results. Suppose we increase the velocity W^* of the particle while all other parameters are fixed; this results in a similar increase of the drag scaling quantity, $\sim W^*$. Hence in this case the statement that the dimensionless drag decreases with Ro means that the physical drag increases slower than linearly with W^*. On the other hand, changing Ro by means of Ω^* does not influence the drag scaling – but affects the value of E.

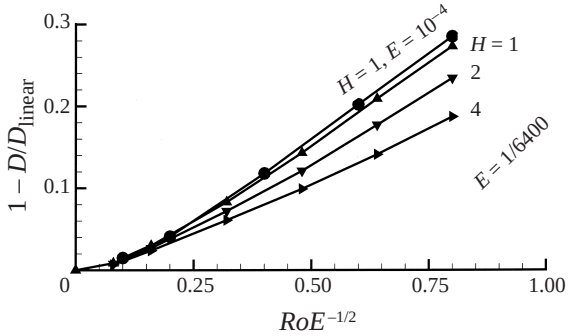

FIGURE 9. The influence of inertial terms on the drag force as a function of $RoE^{-1/2}$ for (*a*) $E = \frac{1}{6400}$, various H, and (*b*) $E = 10^{-4}$, $H = 1$. The values of D_{linear} are: (*a*) 7.24×10^5, 6.62×10^5, 5.79×10^5 for $H = 1, 2, 4$ and (*b*) 1.38×10^6. The points with $RoE^{-1/2} > 0.5$ correspond to an artificial quasi-steady state, whose attainment requires more time than the travel time from the bottom to the midplane.

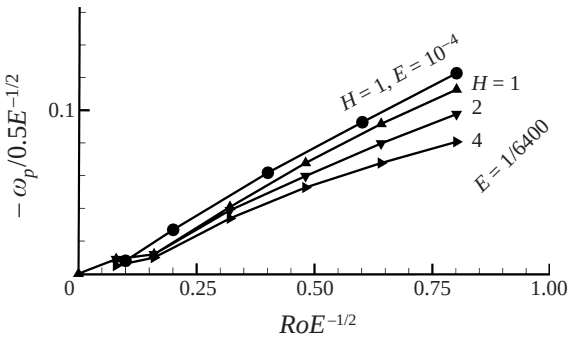

FIGURE 10. The influence of inertial terms on the angular velocity of the particle as a function of $RoE^{-1/2}$, for the parameters given in figure 9.

valid for small values of the parameter $RoE^{-1/2}$. However, these results have not been confirmed by any independent calculation or experiment. We use the present numerical simulations to obtain both verification and more accurate insight into the influence of the nonlinear terms.

We also remark that when $2RoE^{-1/2}$ is not smaller than 1 the assumption of quasi-steadiness of the flow field cannot be fulfilled in physical circumstances, as the particle is displaced more than H during spin-up. In theory, however, it is possible to artificially freeze the position of the particle until spin-up is completed without affecting the boundary conditions. We think that the results of such 'numerical experiments' may provide insights into the contribution of the nonlinear terms athough they lack a clear-cut physical meaning. The drag force during the transient is expected to be lower than in the steady-state. This topic is discussed in the next section.

The influence of increasing Ro on the drag force and on the angular velocity of the particle, ω_p, can be inferred from figures 9 and 10. These graphs summarize results of computation for the configurations: (*a*) $E = \frac{1}{6400}$ and three different values of H, and (*b*) $E = 10^{-4}$, $H = 1$. For each configuration runs with the values of $Ro = 10^{-4}, 10^{-3} - 10^{-2}$ (increment 2×10^{-3}) were performed. We recall that in the core $|\omega| \approx 0.5E^{-1/2}$ and hence the magnitude of ω_p has been scaled with this value. Figure 9 displays the relative difference of the drag from the linear value, $D/D_{\text{linear}} - 1$

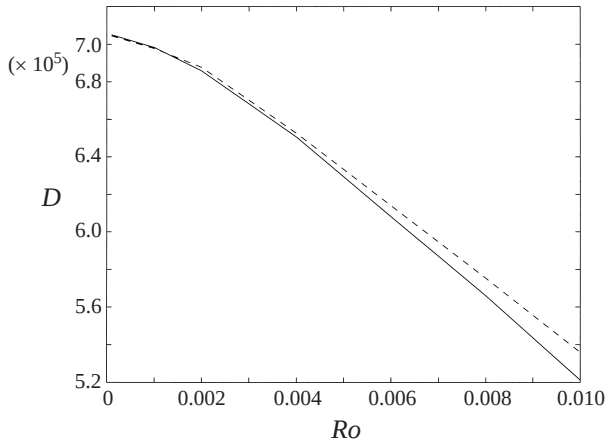

FIGURE 11. The drag force for $E = \frac{1}{6400}$, $H = 1$ as a function of Ro for torque-free (solid line) and rotation-free (dashed line) cases.

as a function of $RoE^{-1/2}$. (The 'linear drag' used for scaling was the force calculated numerically with $Ro = 10^{-4}$.) Figure 10 displays the angular velocity of the torque-free particle, scaled with $0.5E^{-1/2}$ (the approximate value of the angular velocity of the fluid in the core), also as a function of $RoE^{-1/2}$. It is evident that when Ro increases the drag force decreases and that the particle acquires a negative angular velocity. Moreover, we observe that the relative magnitude of these deviations from the 'linear' case is well correlated with the value of the parameter $RoE^{-1/2}$. This parameter can therefore be regarded as the effective Rossby number of the configuration, in the sense that the prominent observable deviations of the flow-field features from the linear case results are quite sharply bounded by the value of this parameter. The alternative candidate for the role of effective Rossby number, $RoE^{-3/4}$, is about 10 times larger for these cases and exceedingly over-restrictive. We also note that the influence of the nonlinear effects decreases slightly when H increases. (Roughly, the behaviour is like $H^{-1/3}$. The detailed influence of H on the nonlinear effects seems to be rather complicated, perhaps involving again the $E^{1/3}$ Stewartson layer. This feature is also consistent with the approximation of Ungarish (1996), but has not been pursued there (see equation (49) in that paper and note that the radial derivative decays with $H^{-1/2}$).) In summary, the present results for deviation from the linear solution correspond to: $D/D_{\text{linear}} \approx 1 - 0.4RoE^{-1/2}H^{-1/3}$ and $\omega_p/0.5E{-}\frac{1}{2} \approx 0.2RoE^{-1/2}H^{-1/3}$.

One major difference between the linear and nonlinear flow concerns the fore–aft symmetry of the flow field. The linear flow in a symmetric domain is symmetric, so the torque-free disk will not rotate relative to the fluid when $Ro = 0$. The flow is expected to lose its fore–aft symmetry in the presence of nonlinear terms and, indeed, the non-zero angular velocity of the disk, see figure 10, is an obvious manifestation of this asymmetry.

Although the appearance of a non-zero ω_p when Ro increases is a significant feature, the contribution of ω_p to the drag force is minor. In other words, the influence of Ro on the drag force is not via the production of ω_p, but rather in parallel with it. We have checked the significance of ω_p on the drag force by comparing the drag force on the torque-free particle (our usual configuration) with that obtained in a computation with a hypothetical rotation-free particle obtained by enforcing $\omega_p = 0$ as a boundary condition. The results for $H = 1$ are shown in figure 11. It can be

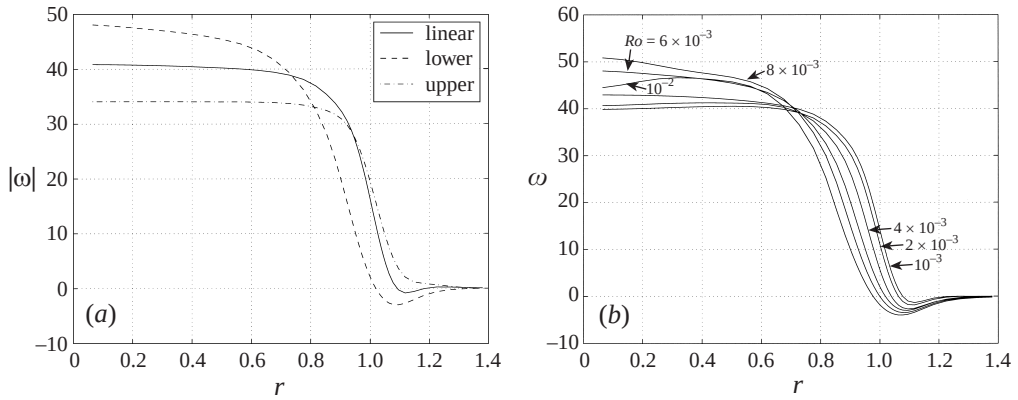

FIGURE 12. The influence of the nonlinear terms on the angular velocity in the core for $E = \frac{1}{6400}$, $H = 1$. $|\omega|$ as a function of r (a) on the upper and lower sides of the particle for nonlinear $Ro = 6 \times 10^{-3}$ (dashed lines) and linear 10^{-4} (solid line) cases; (b) on the lower side for various values of Ro ($1 \times 10^{-3}, 2 \times 10^{-3}, 4 \times 10^{-3}, 8 \times 10^{-3}, 10 \times 10^{-3}$).

seen that the decrease of D is dominated by the increase of Ro, with little difference between the torque-free and rotation-free condition on the particle. For example, for $Ro = 10^{-2}$ although the angular velocity of the particle is about 10% of the angular velocity in the core, the contribution of rotation to the drag force is -2.8%, and the overall contribution of the nonlinear effects is -26% (the non-steadiness will cause an additional decrease). This result supports the conjecture of Ungarish (1996) that the non-zero ω_p has a secondary influence on the drag because it is expected to contribute only via the nonlinear influence of the additional rotation induced by the nonlinear effects, since in the linear case the drag will not be affected if rotation is added to the particle.

The major changes in the flow field that lead to the drag force reduction when Ro is increased can be explained, as in the linear case, by means of the angular velocity profile. Ungarish (1996) pointed out that when Ro increases the vertical shear layers are expected to thicken in the lower region and to contract in the upper region; the corresponding changes in the profiles of ω produce a smaller pressure difference between the upper and the lower sides of the particle than in the linear, symmetric case. This prediction of the quasi-geostrophic model is also confirmed by our computations. Figure 12(a) shows the profiles of the angular velocity in a typical nonlinear case compared to the linear one. Although the deviations from the linear profile are quite pronounced, the resulting effect of the inertial modification on the drag force is quite small because there is a counterbalance of the changes in the upper and lower profiles in the integral which relates the drag force to the angular velocity (quasi-geostrophic nonlinear analogue of (3.29) – equation (50) of Ungarish (1996)). Additional results on the influence of the nonlinear advection terms on the profile of $\omega(r)$ are displayed in figure 12(b).

The influence of the nonlinear terms in a non-symmetrical configuration is similar to that in the symmetrical one. This is illustrated in table 6 for two typical asymmetrical positions of the disk. Again, as Ro increases the drag force decreases and ω_p acquires a retrograde component, but the difference from the linear results is small for small values of $RoE^{-1/2}$.

Finally, we briefly consider the stream lines in the configuration with $E = \frac{1}{6400}$, $Ro = 4 \times 10^{-3}$, $H = 1$, see figure 13. In this configuration $RoE^{-1/2} = 0.32$ and the

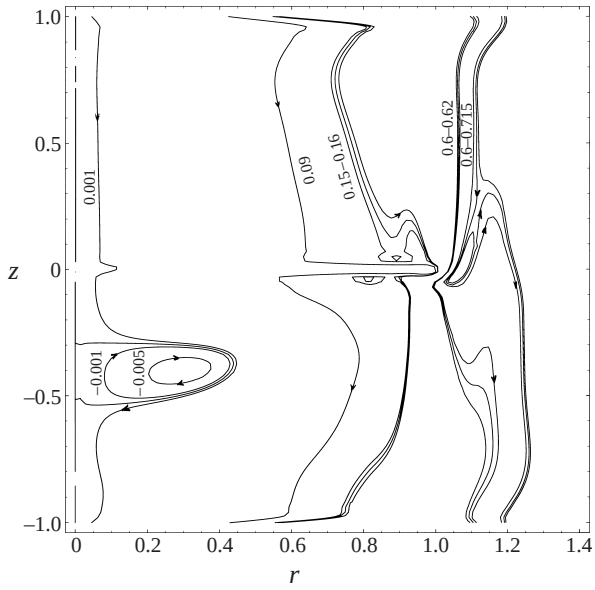

FIGURE 13. The contour lines of the stream function for $E = \frac{1}{6400}$, $H = 1$, $Ro = 4 \times 10^{-3}$.

symmetry between the upper and lower regions is clearly affected by the nonlinear effects, mainly in the Stewartson shear layers. The Ekman layers from which fluid is effluxed (below the upper wall and below the disk) seem to thicken considerably. In addition, a region of recirculation appears in the lower core close to the axis.

We conclude that the results of the investigation of the effect of the nonlinear terms support the prediction of Ungarish (1996) for the range of usefulness of the linear theory, i.e. $Ro\,E^{-1/2} \ll 1$. (The more severe condition of Moore & Saffman (1968) on the usefulness of the linear theory, $Ro\,E^{-3/4}H^{-1/2} \ll 1$, turns out to be over-restrictive.) This conclusion actually rehabilitates the linear theory, because for really small values of E, that can be achieved in practical devices (say, 10^{-4}), the criterion of Moore & Saffman yields impractical restrictions (say, $Ro < 10^{-4}$), about one order of magnitude below the more accurate evaluation. The trends of the influence of the inertial terms on the linear flow field and drag force have been predicted correctly by Ungarish (1996). This strengthens the advantage of the quasi-geostrophic model over the other linear approaches: it provides good insights and the proper trends for a variety of effects without the need to solve partial differential equations. However, the quantitative evaluation of the drag by the quasi-geostrophic model is not accurate. Also, here we detected an additional feature that has been omitted in the previous analysis: the influence of the inertial terms on the drag force is H-dependent (roughly decreases like $H^{-1/3}$ in the cases tested). Consequently, an accurate analytical treatment of the flow field beyond the domain covered by the linear theory is bound to be very complicated, and numerical investigations seem to be the more convenient vehicle for further progress.

4. The time-dependent development of the flow field

The previous theoretical results on the time-dependent velocity field and drag force were asymptotic and had no independent confirmation. We recall that the exact linear solution to the problem of a rising disk corresponds to a steady state only and it is

H_u/H	Ro	$RoE^{-1/2}$	$\omega_p/(0.5E^{-1/2})$	$(D/D_{\text{lin-sym}})-1$	Remarks
0.5	10^{-4}		−0.120	0.0026	
	10^{-3}	0.08	−0.116	−0.0088	
	2×10^{-3}	0.16	−0.116	−0.037	
	4×10^{-3}	0.32	−0.114	−0.101	
	6×10^{-3}	0.48	−0.151	−0.155	
	8×10^{-3}	0.64	−0.165	−0.222	(*a*)
	10^{-2}	0.80	−0.180	−0.283	(*a*)
1.5	10^{-4}		0.104	0.0020	
	10^{-3}	0.08	0.097	−0.0003	
	2×10^{-3}	0.16	0.087	−0.015	
	4×10^{-3}	0.32	0.054	−0.062	(*a*)
	6×10^{-3}	0.48	0.022	−0.119	(*a*)

TABLE 6. The influence of inertial terms on the drag force and the angular velocity of a particle for $E=\frac{1}{6400}$, $H=1$ and two values of H_u/H. $D_{\text{lin-sym}}$ is taken as the drag force computed numerically with $Ro=10^{-4}$ in a *symmetrical* configuration. (*a*) Artificial quasi-steady state, whose attainment requires more time than the travel time from the bottom to the given position.

not clear if and how it can be extended to the time-dependent case. Moreover, to the best of our knowledge, no experimental investigations have addressed this issue. The time-dependent behaviour is obviously influenced by the type of forcing applied to the particle, and two cases seem to be of particular interest: (1) an impulsive start from rest to the final velocity, and (2) a start from rest under the action of a constant force (like a buoyant particle released in a vertical cylinder). The numerical computations are able to provide information on both cases. The simulation of the latter case requires the non-trivial assumption that a very thin disk has a finite (and not necessarily very small) mass, but the results indicate that this has a physically acceptable interpretation.

4.1. *Impulsive start*

Smith (1987) discussed the time-dependent formations of the geostrophic core and of the Stewartson layers in a symmetric configuration. Ungarish (1997) considered the time-dependent problem by both geostrophic and quasi-geostrophic models and obtained explicit expressions for the drag force in these cases. In the following discussion we focus our attention on the behaviour of the drag force, which is more likely to be measured in the experiments than the velocity field. The detailed behaviour of the time-dependent velocity field is beyond the scope of the present work; overall, it appears to be consistent with the predictions of Smith (1987) and Ungarish (1997).

We recall the results of Ungarish (1997) for a disk particle in the midplane position for the geostrophic approximation,

$$D(\tau)=\frac{\pi}{2}E^{-3/2}(1-\mathrm{e}^{-2\tau}), \tag{4.33}$$

and for the quasi-geostrophic approximation,

$$D(\tau)=\frac{\pi}{2}E^{-3/2}\left\{\left[1-4\varepsilon\frac{I_2(1/\varepsilon)}{I_1(1/\varepsilon)}\right]-8\sum_{k=1}^{\infty}\mathrm{e}^{-2(1+\varepsilon^2z_k^2)\tau}\frac{1}{1+\varepsilon^2z_k^2}\frac{1}{z_k^2}\right\}, \tag{4.34}$$

where z_k are the zeros of the Bessel function $J_1(z)$, $\varepsilon=(H/2)^{1/2}E^{1/4}$ and $\tau=t/$

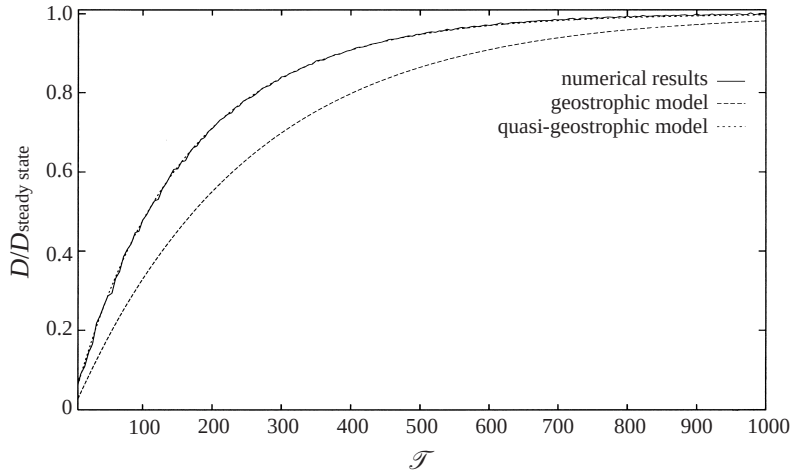

FIGURE 14. The behaviour of the drag force with time for an impulsive start for $E = 10^{-4}$, $H = 5$. $D/D_{\text{steady-state}}$ as a function of $\mathscr{T}(= t^*\Omega^*)$ for geostrophic, quasi-geostrophic and numerical ($Ro = 10^{-4}$) results. Note that the spin-up time interval, $\tau = 1$, corresponds to $\mathscr{T} = E^{-1/2}H = 500$.

$(RoE^{-1/2}H) = t^*\Omega^* E^{1/2}/H$ is the time scaled with the Ekman-layer spin-up interval. According to these results, the presence of the $E^{1/4}$ layers shortens the transient time.

Figures 14 and 15 illustrate, for two different combinations of E and H, the time-dependent behaviour of the drag force as predicted by the geostrophic, quasi-geostrophic and numerical (with $Ro = 10^{-4}$) approaches. For a given configuration all three solutions tend monotonically to a steady state in roughly the same time, which is of order unity on the scaled τ for the different configurations. This confirms the predictions that the essential mechanism in the flow-field adjustment is the Ekman-layer spin-up transport.

An additional interesting feature is shown by these plots. We know from the previous sections that the $D_{\text{steady-state}}$ of the quasi-geostrophic and numerical calculations are not in good agreement. On the other hand, we see that the curves of the time dependence of the scaled value $D(t)/D_{\text{steady-state}}$ for the quasi-geostrophic model and for the numerical computations almost coincide, while the curve for the geostrophic approximation is significantly below for most of the spin-up stage. (This feature has been consistently observed for other combination of parameters not shown here.) This unexpected agreement between the quasi-geostrophic model and numerical computations probably reflects the fact that the $E^{1/3}$ layers are quasi-steady compared to the $E^{1/4}$ layers (see Smith 1987). We therefore speculate that this outcome remains valid in a wide range of practical values of E (and also for non-disk geometries) and allows a good approximation of the behaviour of $D/D_{\text{steady-state}}$ via the use of the simple quasi-geostrophic results (in spite of the fact that the value of $D_{\text{steady-state}}$ itself is not accurately predicted by this model).

4.2. *Constant driving force*

Another case of interest is that of motion from rest under the action of a constant force. This is expected to provide a good approximation to the physical situation of a buoyant particle which is released from rest at some position along the axis of rotation, which is parallel with the gravity acceleration. The experiments of Maxworthy (1968) and of Bush *et al.* (1995) were performed in this way, the former with rigid spherical

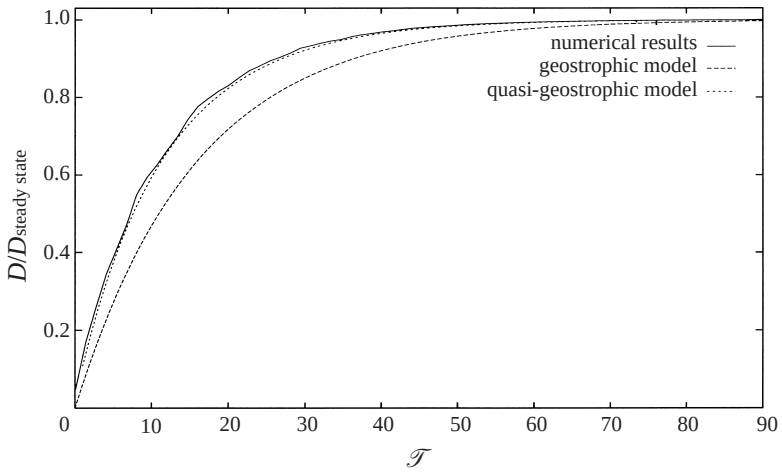

FIGURE 15. Same as figure 14, but for $E = 10^{-3}$, $H = 1$. Note that the spin-up time interval, $\tau = 1$, corresponds to $\mathscr{T} = E^{-1/2}H = 31.6$.

particles lighter than the embedding water and the latter with oil drops in water. Unfortunately, however, almost no record of the initial stage of motion was made, the main concern of these experiments being the (supposed attainable) quasi-steady state.

The only theoretical study of this problem was performed, to the best of our knowledge, by Ungarish (1997). It indicated that the axial velocity of the particle and the drag force on it perform large and rapid oscillations (almost with the inertial frequency $2\Omega^*$) about the steady-state values, and that the amplitudes of the oscillations decay exponentially on the spin-up time scale. However, it has been pointed out during that analysis that some inconsistency between the results and the initial assumptions appears, in particular concerning the z-independence of the pressure. Consequently, these results were considered of qualitative value only and in strong need of verification. Such a verification of the essential behaviour and a more quantitative insight are attempted here with the aid of the numerical computations.

The solution of the present problem requires some changes in the numerical code that has been used in the previous sections: the velocity of the particle relative to the horizontal boundaries, w_p, is now a part of the problem.

For this additional variable we add to the previously used system the standard equation of motion of the particle. The total force acting on the disk is the constant external (say, the effective buoyancy) force minus the instantaneous drag force, $D^*(t^*)$. As in the previous case, we scale the velocities with the particle velocity at the steady state, so the steady state has to be identical to the case of an impulsive start. This means that the external force is equal to the drag force at the steady state, $D^*(\infty)$, which can be computed from the impulsive start configuration. The mass m_p^* of the particle is considered here as a known, controllable, constant quantity. It is obviously positive and, in physical circumstances, restricted by the volume and density of the material, as discussed later. This adds one free parameter to Ro, E and H that govern the flow in the quasi-steady state.

Now we have to solve the Navier–Stokes equations together with the equation of motion for the particle which give the boundary condition for the Navier–Stokes

equations:

$$m_p^* \frac{\mathrm{d}w_p^*}{\mathrm{d}t^*} = D^*(\infty) - D^*(t^*), \tag{4.35}$$

or in dimensionless form

$$m_p \frac{\mathrm{d}w_p}{\mathrm{d}\mathscr{T}} = D(\infty) - D(\mathscr{T}). \tag{4.36}$$

Here, again, $\mathscr{T} = t^*\Omega^*$ and the dimensionless mass is scaled as

$$m_p = m_p^* \frac{\Omega^*}{\nu^* \rho^* a^*}. \tag{4.37}$$

In this scaling, if the dimensional mass of the particle is $m_p^* = A\rho^* a^{*3}$, where A is a non-dimensional positive constant of the order of unity, its dimensionless mass will be $m_p = AE^{-1}$. For example, the dimensionless mass of a spherical particle with the same density as the fluid, ρ^*, is $m_p = \frac{4}{3}\pi E^{-1}$. On the other hand, the right-hand side of (4.36) is $O(E^{-3/2})$ and hence a strong acceleration is expected on the $\mathscr{T}$ time scale. (The paper of Ungarish 1997 uses a different scaling for the mass: to convert, the present m_p should be multiplied by $2E^2/(\pi H)$; this is because the solution in that paper is performed in terms of the τ time coordinate.)

It was found (Minkov 1998) that an explicit discretization of (4.36) destabilizes the numerical solution of the whole problem. A both stable and accurate incorporation of (4.36) is via the implicit discretization:

$$w_p^{n+1} = w_p^n + \frac{\Delta\mathscr{T}}{m_p}\left(D^\infty - \frac{D^{n+1} + D^n}{2}\right). \tag{4.38}$$

This scheme takes into account both acceleration-dependent and flow-field-dependent terms of the drag force since it is dependent on D^{n+1}. However we have to know w_p^{n+1} to compute the flow field and, in particular, the drag force at the time step $n+1$ and (4.38) requires D^{n+1} for computing w_p^{n+1}, so (4.38) must be solved by iteration as follows: the flow field at the ith iteration is based on the ith iteration for w_p^{n+1}, and then, through (4.38), the $(i+1)$th iteration for w_p^{n+1} is computed. For the first approximation for w_p^{n+1} we can use w_p^n. So the iterative solution for (4.38) is as follows:

$$\tilde{w}_0^{n+1} = w_p^n, \tag{4.39}$$

$$D_i^{n+1} = D(\tilde{w}_i^{n+1}), \tag{4.40}$$

$$\tilde{w}_{i+1}^{n+1} = w_p^n + \frac{\Delta\mathscr{T}}{m_p}\left(D^\infty - \frac{D_i^{n+1} + D^n}{2}\right), \tag{4.41}$$

$$w_p^{n+1} = \lim_{i\to\infty} \tilde{w}_i^{n+1}. \tag{4.42}$$

This iteration can be accelerated significantly by use of the simple Aitken extrapolation. We found that typically one step of extrapolation gives about six correct digits, so (4.42) may be replaced by

$$w_p^{n+1} = w_2^{n+1} + \frac{(w_2^{n+1} - w_1^{n+1})^2}{w_2^{n+1} - 2w_1^{n+1} + w_0^{n+1}}. \tag{4.43}$$

The discretization (4.38)–(4.41) and (4.43) was used to obtain the results presented below. We note that this algorithm increases considerably the computational time compared with the impulsive start problem: now the progress of one time step of the

flow-field simulation contains three full cycles of numerical solution of the Navier–Stokes equations. We recall that the acceleration of the origin of the system has been implicitly included in the reduced pressure term and hence the flow-field equations remain in the form used for the impulsive start problem.

Typical results for the drag force and axial motion as a function of time, for $E = 10^{-3}$, $H = 1$, $Ro = 10^{-4}$ and different values of the dimensionless mass m_p, are displayed in figures 16 and 17. The spin-up time interval for this configuration is $\mathscr{T} = 31.6$. We note that for $E = 10^{-3}$ the dimensionless mass of a sphere with the density of the fluid is 4189, see (4.37).

The numerical results reproduce in a clear-cut manner the appearance of oscillations in the axial motion which decay on the spin-up time interval. The frequency of these oscillations increases when m_p decreases, but is smaller than 2 (on the time coordinate $\mathscr{T}$) for all the cases tested. Moreover, we notice that the behaviour of the particle velocity does not depend strongly on the mass for light particles. This can be attributed to the virtual mass effect, i.e. the need to accelerate the fluid becomes the dominant momentum absorber when the mass of the particle itself diminishes. This indicates that the behaviour obtained here for a thin disk is expected to be physically relevant to more realistically shaped particles. The pressure field, not displayed here, is indeed z-dependent.

We emphasize that the actual, physical, magnitude of the oscillations is so small that very special care is needed to observe them. Consider the distance travelled by the particle between the points where the velocity changes sign from positive to negative in figure 17. These positions, where the particle attains a clear-cut position of instantaneous rest, seem an appropriate feature for experimental observations. For $m_p = 100$ the first such point occurs at a distance of about 14 from the release positions, and the next two points follow at intervals of about 5 and 8 on the dimensional scale $Ro\, a^*$; the next points are hard to identify. Hence for small values of Ro (say 10^{-3}) we are concerned with lengths of the magnitude of about 1% of the particle radius. Bush (1993, figure 5.6) shows the measured trajectory z_p as a function of time of a drop of oil of radius of about 2 cm at $Ro \approx 0.01$, $E \approx 3 \times 10^{-4}$, $H \approx 5$ released from rest near the bottom wall in water. For these parameters the amplitude of the oscillations (estimated from the previous disk results) is about 2 mm, below the resolution of the reported measurements. The global measured behaviour is consistent with the theory, but the different properties of the disk and the drop do not allow a quantitative comparison between the present results and these experiments.

The global conclusion from the time-dependent flow cases considered here is that the numerical computations confirm that for both impulsive start from rest with a constant velocity and release from rest under a constant force the time-dependent effects decay on the Ekman-layer spin-up time interval, $E^{-1/2}H/\Omega^*$ in dimensional form. In the case of impulsive start the steady state is approached monotonically, and in the case of start under constant force the steady state is attained within rapid oscillation. A detailed experimental examination of these effects has yet to be performed.

5. Concluding remarks

The flow generated by a slowly rising particle in a rapidly rotating fluid is a classical problem which, after decades of analytical and experimental investigations, still poses many fundamental open questions and doubts about the reliability of the body of knowledge concerning the velocity field and the resulting drag force. The present

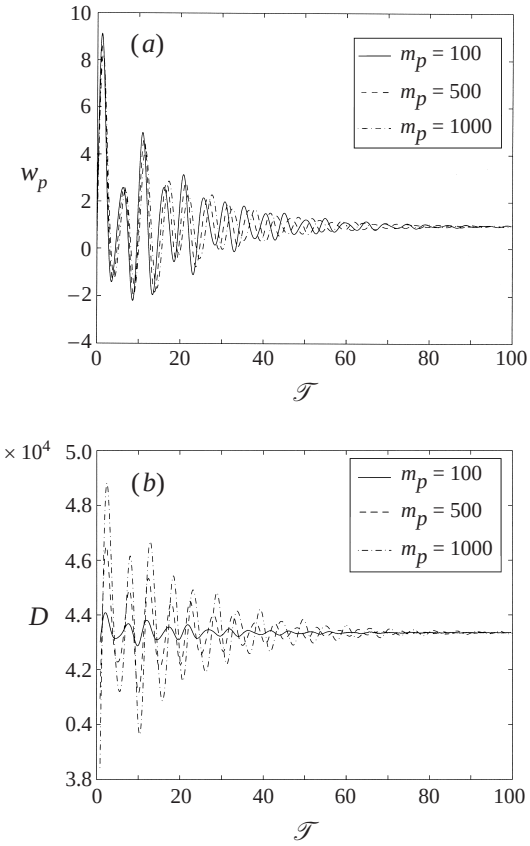

FIGURE 16. (*a*) The particle velocity and (*b*) the drag force as functions of time for motion under constant driving force with $E = 1/1000$, $H = 1$, $Ro = 10^{-4}$, $m_p = 100$, 500 and 1000.

numerical investigation, for a disk particle, seems to close some gaps of knowledge and increase the credibility of earlier inferences. In the present paper attention was focused on the 'short container' configuration for which, to the best of our knowledge, no previous numerical solution has been published. The 'long container' numerical results will be presented in a sequel (Minkov *et al.* 2000).

We have compared the numerical solution for a very small Ro with the disk moving in the centre of the container in a quasi-steady state to the exact linear solution of Ungarish & Vedensky (1995). The comparison, performed for different sets of parameters, shows excellent agreement between the flow fields and the drag forces of the two solutions. This comparison provides confirmation of both the analytical-linear and numerical investigations and dismisses the suggestion of the singularity of the linear problem (i.e. that the behaviour of the flow with a very small Ro may differ significantly from the linear solution obtained with $Ro = 0$). We also performed comparisons with some predictions of the quasi-geostrophic model (Ungarish 1996) and explained the way in which the rather thin $E^{1/3}$ shear layer contributes significantly to the increase of the drag above the prediction of this model.

We also presented solutions with small Ro with the disk in a non-symmetric position.

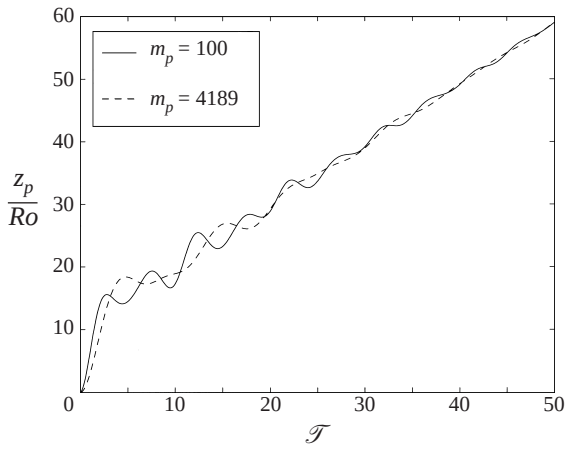

FIGURE 17. The axial displacement (divided by Ro) of the particle as a function of time $\mathscr{T}$ for motion under constant driving force with $E = \frac{1}{1000}$, $H = 1$, $Ro = 10^{-4}$, for $m_p = 100$ and $m_p = 4189$.

By increasing the value of Ro, we checked the influence of the inertial nonlinear momentum advection terms on the flow field and the drag force. We compared this influence with the approximate predictions by the quasi-geostrophic model. The results support the estimates of Ungarish (1996) for the range of usefulness of the linear theory, i.e. $Ro\,E^{-1/2} \ll 1$, and his prediction about the modifications introduced by the nonlinear terms: a (slight) decrease of the dimensionless drag force, a relatively small retrograde rotation of the particle, and a contraction (expansion) of the vertical shear layer in the upper (lower) side. The influence of the inertial terms on the drag force turns out to decay slightly when H increases. The condition of Moore & Saffman (1968) on the applicability of the linear theory, $RoE^{-3/4}H^{-1/2} \ll 1$, was definitively found to be over-restrictive in the range of parameters tested here. We suggest that now there is a quite strong body of evidence, both analytical and numerical, which correlates (and even bounds) the prominent deviations from the linear theory results to the value $Ro\,E^{-1/2}H^{-1/3}$. This finding definitively rehabilitates the importance of the linear theory for attainable small values of E (say, as small $\frac{1}{20000}$) and Ro (say, of the order of 10^{-3}).

We presented results for the time-dependent behaviour of the drag force in the case of an impulsive start. Surprisingly, the ratio of the time-dependent drag force to the steady-state value as a function of time turned out to be the same for the numerically calculated results and for the quasi-geostrophic model. The exact reason has yet to be explained.

We presented an investigation of the time-dependent behaviour for the case of a start from rest of the particle motion under a constant force. The results confirm the qualitative effect of the particle oscillations indicated by Ungarish (1997). The behaviour of these oscillations is dependent on the mass of the particle: for small mass it is quite similar to harmonic and it becomes more complicated when the mass increases. An experimental examination of the oscillation effect has yet to be performed.

Strictly speaking, the present investigation of the short container configuration for small values of the parameter E and small to moderately small values of the parameter $Ro\,E^{-1/2}$ did not provide any revolutionary insights into the behaviour of the flow field and drag force compared with the previous body of theoretical

knowledge. However, we recall that a great deal of that knowledge was based on bold approximations and deductions which had no independent confirmation. The support provided by the present numerical results elevates the available body of information to the status of a reliable theory.

The main deficiency of the present study is the disk shape of the particle. However, this is not expected to alter the main conclusions. For further theoretical progress, and encouraged by the present solutions, it would be interesting to extend the numerical investigations in several directions. First, the change of the particle shape to a sphere or ellipsoid would be very significant for direct comparisons with experimental results. Second, the use of a drop of finite viscosity instead of a solid particle would generalize the problem to multiphase systems. These numerical computations require complex modifications of the present code, or use of different numerical codes, and are beyond the objective of our present investigation.

Beside the incentive for additional numerical results, the conclusion that the linear theory is a quite accurate predictive tool provides increased motivation for seeking additional analytical solutions to the full linear equations of motion.

The present results also indicate that the quasi-geostrophic model approximation (Ungarish 1996, 1997) is a versatile and robust tool which provided the correct parametric trends and insights for steady-state, time dependent and slightly nonlinear cases. This is encouraging, because this model is still the best solution available for spherical and ellipsoidal particles and drops, even in the linear case, and the only approximation available for small but non-zero values of Ro.

The present progress in theory suggest the need of new experiments. For many years the experimental information surpassed and challenged the theoretical knowledge. Now the situation has changed to the opposite. Experimental clear-cut verification of the influence of $Ro\,E^{-1/2}$, asymmetry and time-dependent stage are expected to strengthen our knowledge. Experimental observations on interactions between two (and more) particles are expected to point out novel and perhaps fascinating effects.

The research was partially supported by the Fund for the Promotion of Research at the Technion and by the Bar-Nir Bergreen Software Technology Center of Excellence.

REFERENCES

Bush, J. W. M. 1993 Drop motion in rotating fluids: a model of compositional convection in the earth's core. PhD thesis, Harvard University.

Bush, J. W. M., Stone, H. A. & Bloxham, J. 1992 The motion of an inviscid drop in a bounded rotating fluid. *Phys. Fluids* A **4**, 1142–1147.

Bush, J. W. M., Stone, H. A. & Bloxham, J. 1995 Axial drop motion in a rotating fluid. *J. Fluid Mech.* **282**, 247–278.

Davis, A. M. J. & Stone, H. A. 1998 Slow translation, rotation or oscillation of a disk in a rotating fluid: effect of a plane wall or another disk. *Q. J. Mech. Appl. Maths* **51**, 495–513.

Dennis, S. C. R., Ingham, D. B. & Singh, S. N. 1982 The slow translation of a sphere in a rotating viscous fluid. *J. Fluid Mech.* **117**, 251–267.

Greenspan, H. P. 1968 *The Theory of Rotating Fluids*. Cambridge University Press (reprinted by Breukelen Press, Brookline, MA, USA, 1990).

Karniadakis, E. G., Israeli, M. & Orszag, S. A. 1991 High-order splitting methods for the incompressible Navier–Stokes equations. *J. Comput. Phys.* **97**, 414–443.

Maxworthy, T. 1968 The observed motion of a sphere through a short, rotating cylinder of fluid. *J. Fluid Mech.* **31**, 643–655.

Minkov, E. 1998 A numerical study of the flow around particles in rotating fluid. PhD Thesis, Technion.

Minkov, E., Ungarish, M. & Israeli, M. 2000 The motion generated by a rising particle in a rotating fluid – numerical solutions. Part 2. A long container. In preparation.

Moore, D. W. & Saffman, P. G. 1968 The rise of a body through a rotating fluid in a container of finite length. *J. Fluid Mech.* **31**, 635–642.

Moore, D. W. & Saffman, P. G. 1969 The structure of free vertical shear layers in a rotating fluid and the motion produced by a slowly rising body. *Phil. Trans. R. Soc. Lond.* A **264**, 597–634.

Smith, S. H. 1987 The formation of Stewartson layers in a rotating fluid. *Q. J. Mech. Appl. Maths* **40**, 575–594.

Stewartson, K. 1966 On almost rigid rotations. *J. Fluid Mech.* **26**, 131–144.

Ungarish, M. 1996 Some shear-layer and inertial modifications to the geostrophic drag on a slowly rising particle or a drop in a rotating fluid. *J. Fluid Mech.* **319**, 219–249.

Ungarish, M. 1997 Some spin-up effects on the geostrophic and quasi-geostrophic drag on a slowly rising particle in a rotating fluid. *Phys. Fluids* **9**, 325–336.

Ungarish, M. & Vedensky, D. 1995 The motion of a rising disk in a rotating axially bounded fluid for large Taylor number. *J. Fluid Mech.* **291**, 1–32.